GENETICALLY-TUNABLE MORPHOLOGY AND MECHANICAL PROPERTIES OF BACTERIAL FUNCTIONAL AMYLOID NANOFIBERS

A THESIS SUBMITTED TO

THE GRADUATE SCHOOL OF ENGINEERING AND SCIENCE

OF BILKENT UNIVERSITY

IN PARTIAL FULFILLMENT OF THE REQUIREMENTS FOR

THE DEGREE OF

MASTER OF SCIENCE

IN

MECHANICAL ENGINEERING

By

Mohammad Tarek Hamed Abdelwahab

May, 2017

GENETICALLY-TUNABLE MORPHOLOGY AND MECHANICAL PROPERTIES OF BACTERIAL FUNCTIONAL AMYLOID NANOFIBERS

By Mohammad Tarek Hamed Abdelwahab

May, 2017

We certify that we have read this thesis and that in our opinion it is fully adequate, in scope and in quality, as a thesis for the degree of Master of Science.

Mehmet Zeyyad Baykara (Advisor)

Emine Yegan Erdem

Mehmet Fatih Danışman

Approved for the Graduate School of Engineering and Science:

Ezhan Karaşan

Director of the Graduate School

ABSTRACT

GENETICALLY-TUNABLE MORPHOLOGY AND MECHANICAL PROPERTIES OF BACTERIAL FUNCTIONAL AMYLOID NANOFIBERS

Mohammad Tarek Hamed Abdelwahab

M.S. in Mechanical Engineering

Advisor: Mehmet Zeyyad Baykara

May, 2017

The highly dynamic behavior of material systems exploited by nature results in research efforts to employ them as next generation biomaterials exhibiting sustainability and resistance against harsh environmental conditions. In recent years, functional protein-based structures started to be investigated heavily. Among these, bacterial biofilms present themselves as highly organized, hierarchical, dynamic material systems comprising cells, various carbohydrates, and extracellular proteins. They are known to be resistant against different kinds of disruptions by chemical, physical, and biological agents. These fascinating qualities make them potential candidates for next generation biomaterials.

Motivated as above, we present in this M.S. thesis a comprehensive study of the morphological and mechanical properties (in terms of Young's modulus) of biofilm structures assembled from bacterial amyloid nanofibers of *Escherichia coli* (*E. coli*) via imaging and force spectroscopy performed by the atomic force microscope (AFM).

We used techniques adopted from genetic engineering to employ different *E. coli* mutants, allowing comparisons of Young's modulus and morphology of different biofilm nanofibers based on genetic composition. In particular, we tuned the genetic expression of the major (CsgA) and minor (CsgB) proteins constituting bacterial amyloid nanofibers, with the optional addition of certain amino acid tags in order to

have multiple controlled versions of biofilm nanofibers. After sample preparation, we calibrated a *single* AFM probe to be used for all experiments, and performed contact-mode imaging measurements to probe the morphological differences among these genetically-different biofilm amyloid nanofibers. In addition, we conducted nanoindentation experiments to obtain force spectroscopy curves. A precise processing routine was developed to extract the mechanical stiffness from acquired data. Furthermore, we statistically contrasted the stiffness values to reveal the genetic dependence of the mechanical properties of the final protein assembly. The processing routine was also able to detect the effect of the substrate on mechanical stiffness measurements.

The experimental results presented in this thesis pave the road for the use of genetic engineering to rationally tune the mechanical as well as the morphological properties of bacterial amyloid nanofibers, and thereby underline the critical role that they may play as new generation biomaterials.

Keywords: Biofilm Proteins, Amyloid Nanofibers, Atomic Force Microscopy, Force Spectroscopy

ÖZET

BAKTERİYEL AMİLOİD FONKSİYONEL NANOFİBERLERİN GENETİK OLARAK AYARLANABİLİR MORFOLOJİ VE MEKANİK ÖZELLİKLERİ

Mohammad Tarek Hamed Abdelwahab

Makine Mühendisliği, Yüksek Lisans

Tez Danışmanı: Mehmet Zeyyad Baykara

Mayıs, 2017

Doğa tarafından kullanılan malzeme sistemlerinin yüksek derecede dinamik davranışı, onları sert çevre koşullarına karşı sürdürülebilirlik ve direnç gösteren yeni nesil biyomalzemeler olarak kullanmak adına gerçekleştirilen araştırma çabalarını ortaya çıkarmaktadır. Son yıllarda fonksiyonel protein temelli yapılar yoğun olarak araştırılmaya başlanmıştır. Bunlar arasında, bakteriyel biyofilmler; hücreler, çeşitli karbonhidratlar ve hücre dışı proteinler içeren iyi derecede organize edilmiş, hiyerarşik, dinamik materyal sistemleri olarak ortaya çıkmaktadır. Bakteriyel biyofilmlerin; kimyasal, fiziksel ve biyolojik ajanlar tarafından yol açılabilecek çeşitli bozulmalara karşı dirençli oldukları bilinmektedir. Bu etkileyici nitelikler, bakteriyel biyofilmleri yeni nesil biyomalzemeler için potansiyel adaylar haline getirmektedir.

Yukarıda belirtilen düşüncelerden yola çıkarak; bu M.S. tezinde, atomik kuvvet mikroskobu (AFM) ile gerçekleştirilen görüntüleme ve kuvvet spektroskopisi deneyleri vasıtasıyla, *Escherichia coli* (*E. coli*)'nin bakteriyel amiloid nanofiberlerinden oluşan biyofilm yapılarının morfolojik ve mekanik özellikleriyle ilgili (Young modülü açısından) kapsamlı bir araştırma sunuyoruz.

Biyofilm nanofiber Young modüllerinin ve morfolojilerinin genetik yapıya dayanarak karşılaştırılmalarını sağlayan farklı *E. Coli* mutantlarının oluşturulması amacıyla genetik mühendisliğinden alınan teknikleri kullandık. Özellikle, biyofilm nanofiberlerinin birden fazla kontrollü versiyonuna sahip olmak adına, bakteriyel amiloid proteinleri oluşturan majör (CsgA) ve minör (CsgB) proteinlerin genetik ifadesini, belirli aminoasit etiketlerinin opsiyonel olarak eklenmesiyle ayarladık. Numuneler hazırlandıktan sonra, tüm deneyler boyunca kullanılacak olan tek bir AFM ucunu ölçülendirdik ve genetik olarak farklı biyofilm amiloid nanofiberleri arasındaki morfolojik farklılıkları derinlemesine incelemek adına temaslı kipte görüntüleme ölçümleri gerçekleştirdik. Buna ek olarak, kuvvet spektroskopisi eğrileri elde etmek adına nano-indentasyon deneyleri gerçekleştirdik. Elde edilen veriden mekanik rijitliği çıkarmak amacıyla, hassas bir işleme rutini geliştirdik. Ayrıca, nihai protein yapısının mekanik özelliklerinin genetik bağımlılığını ortaya çıkarmak için rijitlik değerlerini istatistiksel olarak karşılaştırdık. İşleme rutini, ayrıca, alt taşın mekanik rijitlik ölçümleri üzerindeki etkisini de tespit edebildi.

Bu tezde sunulan deneysel sonuçlar, bakteriyel amiloid nanofiberlerin mekanik ve morfolojik özelliklerinin rasyonel olarak ayarlanmasında genetik mühendisliğinin kullanımının yolunu açmakta ve böylece yeni nesil biyomalzeme olarak oynayabilecekleri kritik rolü vurgulamaktadır.

Anahtar Kelimeler: Biyofilm Proteinleri, Amiloid Nanofiberler, Atomik Kuvvet Mikroskopisi, Kuvvet Spektroskopisi

Acknowledgement

I want to express my endless gratefulness to my academic advisor Prof. Mehmet Zeyyad Baykara for his guidance, patience, understanding and trust. I never imagined my supervisor would be that thoughtful and helpful such that I had been called “lucky” so many times because I am his pupil, which I always admit happily. I would like to thank him for all the time he spent with me in his office teaching me the craft of research and either listening to my “crazy” ideas directly or reading them in excessively long emails and even replying to them in detail, not to forget his careful readings of my work. I hope the time will come to repay him by honoring his name but that time should not be by words but by making him proud hopefully few years from now, or as Nietzsche put it: “One repays a teacher badly if one always remains nothing but a pupil.” So, I hope I repay him “well” in the future …

I would like to thank my mother for her support which I would like to postpone talking about to a more suitable place where a larger audience is present …

I was again lucky to meet highly-skilled researchers who are members of our Scanning Probe Microscopy (SPM) research group. As such, I would like to thank Arda Balkancı, Tuna Demirbaş, Ebru Cihan, Alper Özoğul, Berkin Uluutku, Zeynep Melis Süar, Verda Saygın and Nasima for their enlightening discussions, support, amusing chatting and friendship. I hope they all achieve all their dreams in the future and be happy and cheerful, as always.

I have met many valuable friends at Bilkent who encouraged me and gave me company all along the way. So, I would like to thank Tamer, Ahmed (Konan), Yahya, and the nicest ever couples: Mohamed & Nour, Salman & Elif and Nabeel & Maha for being a family here for both me and my mother. I hope our cheerful, deep, and sometimes silly but light-hearted conversations last as good memories on the hope of meeting again whenever our life roads cross over. I wish all of them enjoyable lives full of love, real happiness, loud laughs, tasty food and non-stopping success.

Bilkent University is a place I called “Home” for more than two years now. So, I would like to thank all the officials of all ranks who are responsible for keeping this place organized, well-equipped and running.

Last but not least, I feel like “Peter Pan” who received at last his own “fairy” (“-Zana”) with her new “road” (“Er-”) which turned life into a magical world with a future full of hope, amicability, “tranquility”, “affection” and “mercy”.

To my mother

Contents

List of Figures

List of Tables

Chapter 1

Introduction

1.1 Overview

Microscopy techniques can be regarded as one of the main driving forces for the fast progress in the last few decades in various fields. For instance, Richard Feynman was amazed in his famous lecture at how fast the biology field was advancing at that time because of microscopy techniques [1]. He argued that all fundamental questions raised by biologists can be fairly answered in a simple way: “you just look at the thing!”. He claimed that what biologists needed at that time is just to “make the electron microscope 100 times better”. Though his imagination took him so far to speculate where the miniaturization potential can take us, biologists nowadays not only look at the biomolecules and the associated biological machinery with very high spatial and temporal resolution but they also manipulate very delicate bio-processes, induce local and controlled changes with various techniques at different scales, in addition to conduct modification experiments on the biological systems under study and collect enormous amounts of crucial data for more in-depth understanding [2-5]. Hence, biologists are no longer “spectators” of nature and this is culminated in their dream to synthesize a whole cell with all its machinery from scratch [6]. And to do so, biologists

depend heavily on knowledge gathered using a variety of microscopy techniques to probe the cellular dynamics of the involved biomolecules at the micro- and nano-scale.

To “stand on the shoulder of the giants” (the motto of the scientific research), we should first see how high those “shoulders” reached. Thus, a brief history of microscopy techniques is provided below.

1.2 History of Microscopy

Humanity’s interest in the universe and themselves reached fairly fast to an unstoppable level of curiosity. This universe shows its marvels on multiple scale levels. Some details are seen via the naked eye, while others need certain equipment to be magnified; although the celestial bodies (e.g. planets) are relatively massive in size, all of them are far enough to be seen in detail via the naked eye. Hence the *telescope* was a crucial invention. On the other hand, there is another world that lies *beneath* our vision scale which seems to govern many processes in our daily lives. Although much closer to us than planets, this world is so minute in scale that our eyes can’t unravel any of its curious details. Thus, the invention of the *microscope* was vital and necessary.

1.2.1 Light Microscopy

For many years, the microscopy field was mostly consisting of light microscopy. Not all people know that Galileo designed at the very beginning of the 16th century his own *Occhialino* (which in Latin means ‘little eye’, referring to the *microscope* concept of looking at small objects) [7-8]. Some even claim that Galileo devised his own microscope (Figure 1.1 (a)) before inventing his outstanding telescope (Figure 1.1 (b)) that famously spotted the craters on the moon and the satellites of Jupiter, while others claim that he just made modifications on the design of Lippershey from a year ago [5, 9].

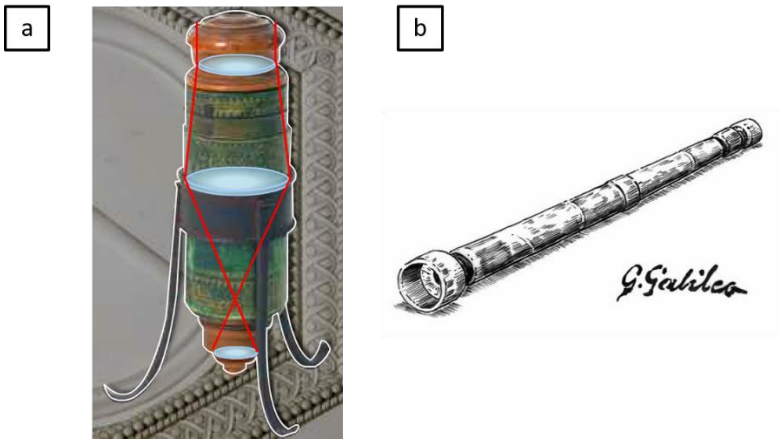

Figure 1.1 Schematics of Galileo's (a) microscope and (b) telescope [10].

Regardless of its origin, the telescope and the microscope share mostly the same configuration; they are basically consisting of similar lenses with multiple surface curvatures (i.e. convex or concave). Nevertheless, the main difference between them lies in the relative spacing between the lenses and their own sizes, thus resulting in a difference in function. Because of the image distortions away from the center of the lens, light microscopes needed smaller lenses, which resembled quite a challenge to be grinded at that time, coupled with the difficulty in their simultaneous alignment with other lenses in the case of *compound* microscopes where multiple lenses exist. These obstacles precluded the use of microscopes in revealing the micro-world for around 30 years until the first documented microscopic image came as a detailed drawing of a certain bee species in, astonishingly, a book of poetry [11]. Another 30 years passed till Robert Hooke designed his own compound microscope in 1665 and published his outstanding book "Micrographia" showing a detailed record of his studies supported by impressive drawings belonging to, e.g., the fly's eye, various insects, bird feathers and other marine organisms [12]. He, most importantly, reported an illustration showing the cork *cells*, which he ironically did not recognize at all; he only coined them with the term "Cell" for the graphical similarity, he saw, with the 'cells of the honeycomb' (Figure 1.2 (b)).

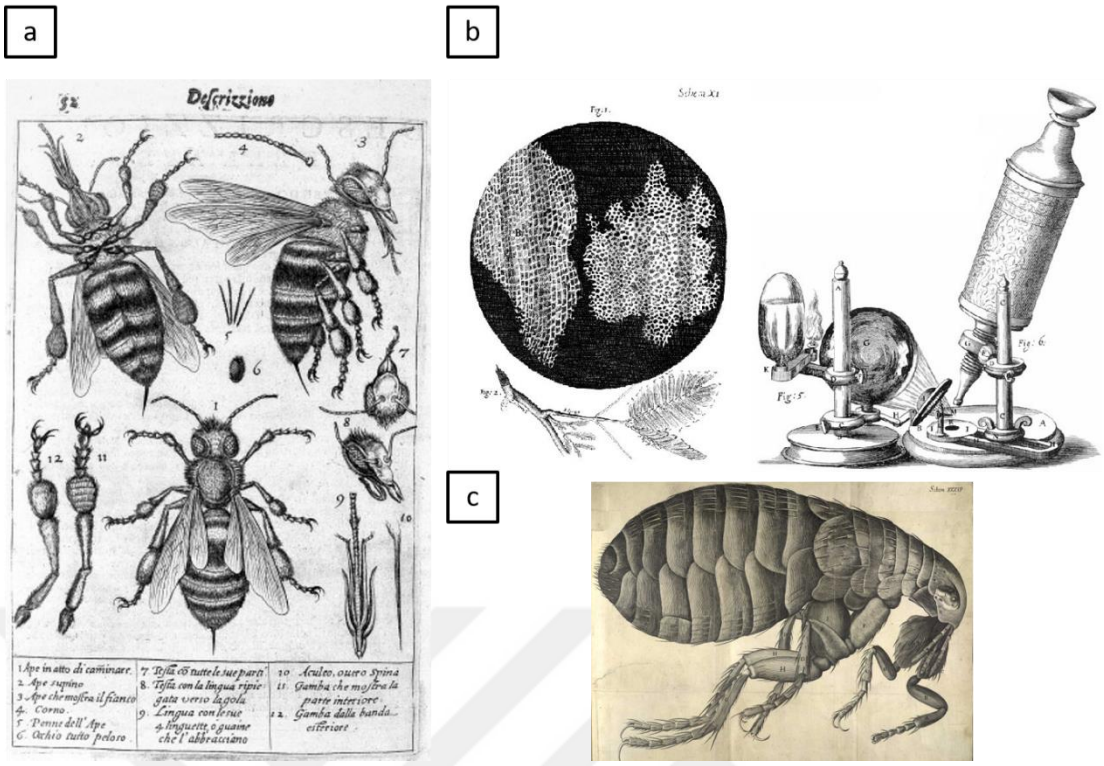

Figure 1.2 Early microscopy images. (a) First credited microscope image belongs to bee insects [11]. (b) Robert Hooke's microscope (right) and his first documented observation of "cells" (left). (c) Flea insect image under Hooke's microscope [12].

Being still hindered by the lens-making challenges, it was not until 1700 that significant magnification (270x) took place in the field of microscopy by the "Father of Microscopy and Microbiology", Van Leeuwenhoek, who cleverly grinded and polished a small lens to be used in a *simple* microscope (i.e. a microscope with one lens) as seen in Figure 1.3 (a). He observed for the first time the "animalcules" (i.e. microorganisms) such as bacteria shown in Figure 1.3 (b). His simple microscope configuration was so powerful that it was still used till the middle of the 19th century. Although it was a remarkable progress, it wasn't reliable enough; the microscope required mounting of the specimen on a needle-like holder situated just in front of the lens, where one's eyes should be away from the lens by only a 1-cm distance.

Figure 1.3 The first observation of microorganisms. (a) Van Leeuwenhoek's microscope. (b) The "Animalcules" (or microorganisms) observed [13].

Hindered by the often-laborious handling of microscope, scientists needed to give one more look backward and try to tackle the instrumental challenges posed by the compound microscope setup with its multiple-lenses configuration. Around a century has passed until Joseph Lister in 1824 tackled the achromatic aberrations involving different focal planes for different wavelengths by designing the two-material type lens [14]. Subsequently, Schleiden and Schwam laid the foundation of the cell theory in 1838 and then came Ernst Abbe in the 1880s who optimized the resolving power of lenses through his grinding and sanding skills and developed the diffraction limit equation [15-17]. Afterwards, artefacts introduced by sample illumination such as glares and bulb filament images on the final image were overcome by August Köhler through his implementation of an auxiliary optical setup at the source side providing even illumination at sample surface with no constraints on the light intensity (i.e. Köhler Illumination) [18]. These breakthroughs constitute the cornerstone of old and modern versions of optical microscopy techniques.

Only by the end of the millennium, new light microscopy techniques started to "break" the diffraction barrier. These techniques were developed with the help of genetics which progressed to develop efficient ways in modifying the DNA reliably. This permitted any protein of interest to have fluorophores (i.e. fluorescent protein reporters) in its genetic construct which make the targeted protein fluorescent by itself, and thus easily tracked and imaged [19].

1.2.2 Electron Microscopy

Motivated by the diffraction limit in optical microscopy and the invention of the electromagnetic lens devised by Hans Busch, Enrst Ruska used the electrons as his source of illuminating radiation and built his own prototypes in 1930s. These prototypes exceeded the resolution achievable by the light microscopy at that time [20].

There are two main types of electron microscopes: the transmission electron microscope (TEM) and the scanning electron microscope (SEM). Their underlying principles are slightly different; in the case of TEM, the whole surface of the sample is subjected to electrons where the ones crossing the nm-scale-thick sample will diffract, carrying information about sample structure. These transmitted electrons are then magnified by the electromagnetic lens and get collected by appropriate detectors to generate diffraction patterns. In the case of SEM, not all regions on the sample surface are subjected to incoming electrons; an accelerated beam of electrons (i.e. *primary* electrons) is focused onto a single spot on the sample surface of typical diameter less than 10 nm and scanned in a "raster" manner. The interactions between the incoming electrons and surface atoms will lead to either elastically (*backscattered*) or inelastically (*secondary*) scattered electrons which are then collected and analyzed by the appropriate detectors (Figure 1.4). If backscattered electrons are collected and processed, the chemical composition of the sample surface can be determined. On the other hand, secondary electrons hold information about the sample topography [21].

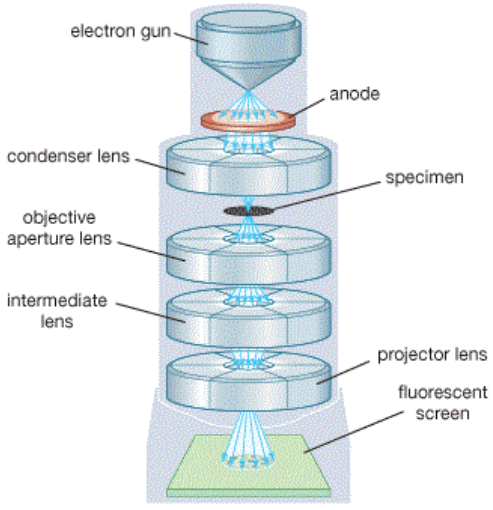

Figure 1.4 Scanning electron microscope (SEM) setup and components [22].

TEM is concerned with revealing the interior (i.e. bulk) structure of a wide variety of biological samples like tissues, micro-organisms, cells, organelles and protein arrangements inside cell membranes. On the other hand, SEM deals with the sample surface, specifically its topography and chemical composition.

Despite their crucial roles in the world of microscopy today, TEM, for instance, requires sectioning of the bulk samples into very thin layers (not larger than 100 nm) so that the transmitted electrons can pass easily. SEM, on the other hand, typically needs several preparation steps like metal coating of insulating materials which is necessary for preventing the samples from being charged and damaged during imaging. There are other laborious procedures needed to prepare most biological samples, including stabilizing the sample through dehydration and fixation by certain chemicals. Moreover, almost all electron microscopes need a vacuum environment such that the electrons are not scattered by the molecules in the ambient atmosphere.

It was not, astonishingly, until 1986 that Ernst Ruska was awarded the Nobel Prize for building the first electron microscope, which was regarded as "an extension of the human eye" by the Royal Academy of Sciences. Still, he was awarded only half of it while the other half was awarded to two scientists who employed sharp *probes* to get close enough to sample surfaces to interact with them through forces and tunneling currents. This approach constitutes the main working principle of the *Probe Microscopy* family.

1.2.3 Probe Microscopy

It was always the dream of scientists to build microscopy techniques with atomic resolution facilitating the observation and even, the "manipulation" of single atoms. This was not achievable yet in the period of 1960's to 1980's either through light microscopy or electron microscopy techniques. Thus, instead of using sub-atomic particles (e.g. photons or electrons) to interact with the samples, researchers came up with the idea of using very sharp *probes* (i.e. extremely fine "needles") to be employed in "feeling" (i.e. interacting with) the sample in the same way we use our finger tips to recognize what is around us, say in a dark room [23].

This way of thinking was first paved by the stylus profilometry technique which was previously used to estimate some surface properties like topographical roughness. Its working principle is very closely related to the phonograph (or turntable) in which a stylus (i.e. sharp probe) is being moved over a surface and thus suffers deflections/vibrations due to topographical features (i.e. valleys and hills). These vibrations modulate on the top of the stylus the distance between two fixed magnets and a sandwiched movable coil. This modulating distance will result in variations of the current generated in the coil, thus registering the information about the feature sizes while scanning [24].

Russell Young used the concept of the needle to build his microscope (*topografiner*) which generated the first image of a sample topography by probe mapping. He applied bias voltage between the tip (or the field emitter) and the conducting surface in order to generate field-emission current between them. The emitter-sample distance was on the order of nanometers and the applied voltage was somewhat high (tens of volts). The generated current was strongly dependent on the emitter-sample distance which was maintained by a servo loop mechanism. This feedback system served to keep this distance constant as much as possible while scanning by adjusting the voltage of the vertical piezo so that it moves to preserve a constant field-emission current. Still, the thermal instability and the mechanical vibrations that this system suffered from prevented the system to hold the current constant for multiple seconds. This prevented the method from detecting a much more delicate but very sensitive phenomenon that holds the key to unravel single atoms, namely: *Quantum Tunneling* [23, 25].

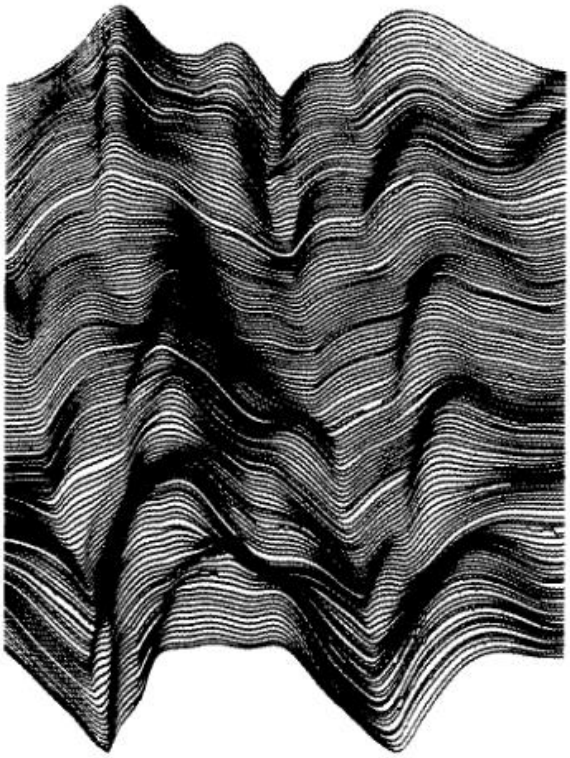

Figure 1.5 Early topography image taken by one of the first probe microscopes (Topografiner) [26].

The quantum tunneling phenomenon involves electron transfer between two atoms which can occur when a (semi-)conducting, sharpened tip (sharpened to the extent that at its foremost end, it will have only one or very few atoms) approaches a (semi-)conducting sample surface very closely. If a bias voltage is applied between tip and sample, electron transfer can be induced over the vacuum barrier, despite the fact that the tip and sample are not "touching". The tip-sample distance must be typically maintained below a nanometer to have quantum tunneling, and thereby measurable electric current. Because of its exponential distance dependence, tunneling was a very appropriate mechanism to be used as a microscopy technique aimed at high spatial resolution (Figure 1.6) [27]. This gap-sensitive method required very precise (sub-nm-scale) mechanical control of the vertical position of the tip above the surface, which can be regarded as the piece-de-resistance that Gerd Binnig and Heinrich Rohrer mastered and achieved in their *scanning tunneling microscope* (STM). Based on this invention, it they were awarded the Nobel Prize in 1986, together with Ernst Ruska for his TEM invention.

It took Binning and Rohrer less than a decade (1979-1986) to perfect the STM by solving diverse problems and to convince the scientific community that their microscope can take accurate images on the atomic scale based on the quantum tunneling effect. They tackled various issues such as reducing mechanical vibrations from the surroundings via mechanical suspension. In addition, they updated their setup with an acoustic hood to damp any acoustic noise. Initially, they faced problems in replicating their own scans. They argued that the reason was tip wear and thus they started working on sharpening the tip before each scan using high electric fields. Helped by their instrumental improvements, Binning and Rohrer provided images of different surfaces like Si of different crystallographic, as shown in Figure 1.7 (a). The final blow to doubts aroused in the scientific community was when Binning and Rohrer used their updated pocket-size STM to compare their atomic-scale images of graphite with its electronic structure which was easily calculated from theory, as seen in Figure 1.7 (b). This was when the STM "matured from an art to a technique" [23].

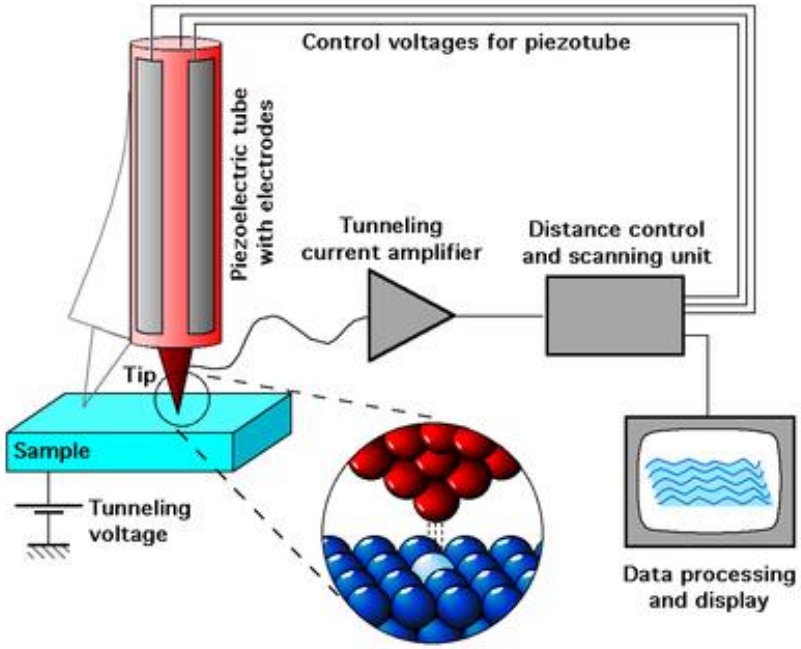

Figure 1.6 STM setup basic principles and components [28].

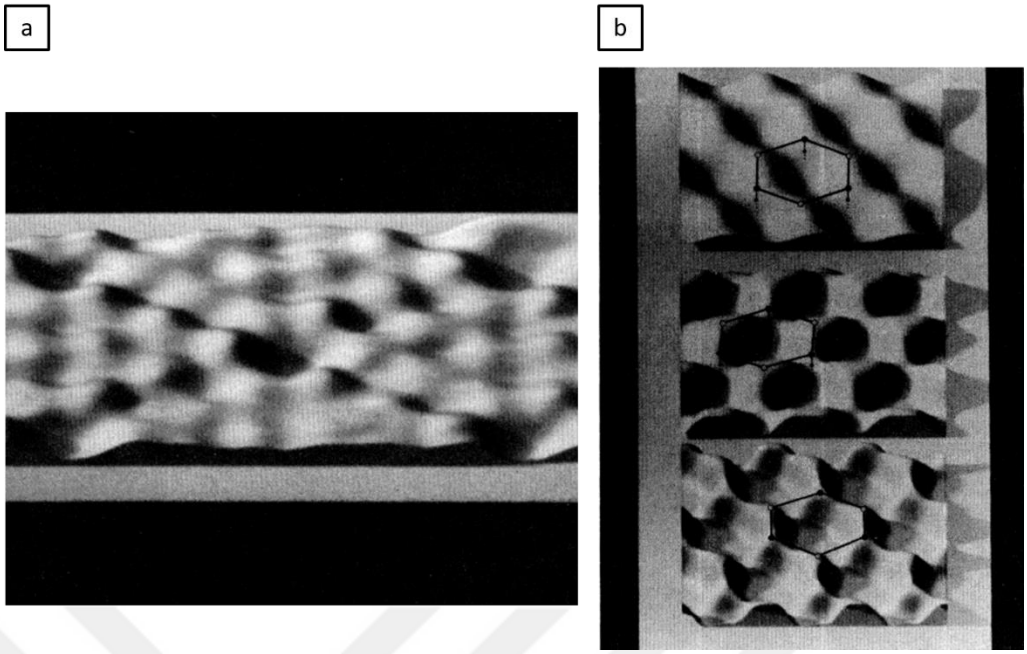

Figure 1.7 Scanning Tunneling Microscope (STM) images of (a) Si (111) and (b) Graphite surfaces [23].

Although the STM made the scientists achieve their dream of "seeing" atoms, it could not be applied to all samples as it requires (semi-)conductivity for the effect of quantum tunneling to occur. This summoned and inspired the rise of a new microscopy technique that could image both conducting and non-conducting samples in air, liquid and vacuum environments, namely *atomic force microscopy* (AFM).

1.3 Atomic Force Microscopy

Atomic force microscopy (AFM), since its invention in 1986 [29], has overcome most of the limits associated with previous microscopes and also exceeded the "modest" dreams of just observing biomolecules and microorganisms at work. AFM has become much more revolutionary, in a sense it doesn't only image with unpreceded spatial resolution but its nature of probing samples facilitated its ability to "interfere" widely with the processes being imaged and conduct measurements (i.e. spectroscopy) to quantify nanoscale properties associated with bio-macro-(nano-)molecules in their own native environment (i.e. liquid), with no considerable damage to the samples.

Combining the profilometry and the STM concepts, AFM utilizes an extremely sharp tip to laterally scan the sample surface under *light* contact thus generates topography images on different kinds of sample surfaces with sub-nm resolution. The sharp tip itself is attached to a micro-manufactured *cantilever* employed as a soft spring (with typical spring constant values below 1 N/m), which exhibits deflections in response to interaction forces arising between the tip and the sample during scanning. Using an optical setup, the minute deflections and hence, forces acting on the probe can be precisely measured (with sensitivity in the sub-nN regime). Feedback loops adopted from STM are employed to keep the tip-sample interaction forces at a constant value while scanning so that high-resolution images of sample topography are generated [30]. We will discuss the basic principles of AFM imaging together with force spectroscopy in Section 2.1.

AFM has made many cross-roads with so many fields like microbiology, immunology, biophysics, nanotechnology, and nanobiotechnology due to its very relaxed limitations on specimen choice, imaging environment, and easy sample preparation steps [31]. In that context, AFM has overcome the hardships in biology which the scanning tunneling microscope (STM) has suffered from [31], by combining the STM feedback capabilities with the profilometer advantages in a new scheme [29]. Once it was shown that the AFM can be used in imaging under fluidic environments [32-34], the doors were wide-open in front of many candidates from the biology world to be studied excessively [34-47]. For instance, AFM was exploited to investigate different kinds of bacteria [36, 43], filamentary structures [44], cell membranes [45], single proteins [37], as well as viruses [46] and genetic materials (Chromosomes and DNA) [39]. By functionalizing the AFM probe with nanoparticles and proteins, and approaching outer cellular membranes, even protein-cell interactions can be probed *in-vivo* [47].

Coming to the ability of force spectroscopy (i.e. probing the sample's nanoscale mechanical properties), it was shown that AFM cannot only "feel" the sample as a nanoscale "finger" to image it, but it is also able to "press" on it to determine the mechanical properties of the sample. For instance, it can be used to probe the adhesive properties of samples contributing as main players in the mechanonanobiology field, giving us more insight into the structure-function relationships in adhesion [48-49]. Also, through the data (i.e. force-distance (FD) curves) collected by the AFM's

“pressing” capability, differentiation between healthy and cancerous cells was possible [50]. Also, through tip “functionalization”, which is a major capability of AFM, force spectroscopy can detect and quantify mechanically the interaction between antibiotics and bacterial cell walls [51]. Functionalizing the tip with chemical groups (called chemical force spectroscopy) enables AFM to be chemically sensitive by mapping, for example, how strong the local receptors on the cell surfaces interact with specific chemicals on the tip, thus providing a deep look into the structure-function properties of the cells [52]. One of the most interesting applications of the tip functionalization is that it can quantify the intermolecular forces between the ligands and their receptors [53-55]. In the previous decade, new approaches that involve the simultaneous use of AFM with other imaging techniques have been invented. For instance, together with confocal microscopy (a type of light microscopy), AFM can probe the stiffening property of metastatic cancer cells before invasion [56]. Also, “correlative imaging” is possible while combining optical techniques with AFM to reveal physical links between different phenomena [57].

Due to the short time scales in which the dynamics of the biological processes change, fast AFMs (usually called high-speed AFMs, or simply HS-AFMs) have been developed in order to image (and in some cases, generate stiffness maps for) different biological samples like the famous Myosin V protein [58]. HS-AFMs also provide video-rate imaging of the dynamics of nanoscale structures such as various proteins associated with the cell membrane and antibodies [59-61].

Pressing our finger against a surface to see if it is hard or soft is a ubiquitous act that is developed as an efficient and crucial ability for our survival by making use of the materials around us. In the case of nanoscale materials, this ability can be mimicked by a “nano-finger” which is the AFM tip employed for indenting the samples under investigation and quantifying their stiffness. The pressing of the tip into the sample (coined as a “nanoindentation” experiment) results in the acquisition of a Force-Piezo Displacement curve or shortly, a force-distance (FD) curve. Through the processing of FD curves, employing theoretical contact models, certain mechanical properties of the sample can be extracted. As such, nanoindentation experiments have been performed in the past over a large variety of biological systems [34, 42, 44, 48, 56, 62].

One of the various biological samples that can be studied using AFM is amyloid nanofibers. It will be necessary and logically fundamental for the reader to be provided with a brief background about the specific biological system investigated in this thesis (i.e. bacterial functional amyloid nanofibers) before we delve into the experimental part in the next chapters and contemplate on the results obtained.

1.4 Amyloid Nanofibers

Amyloid aggregates present a class of thread-like and filamentous morphologies that can be accessed by several globular (particle-like) proteins of various amino acid sequences. Historically, they are known for their notorious association with a variety of chronic neurodegenerative diseases including the Alzheimer disease [63]. Amyloid formation is a polymerization process where soluble proteins can be transformed, through aggregation phenomena under certain (controlled or not) circumstances, to highly-ordered and/or misfolded hierarchical fibrillar structures in the extracellular environment [64].

Structures of amyloid proteins like Sup35, insulin, amyloid-beta peptide (Aβ), Tau, amylin, and prion protein were revealed [65-69]. There are some common characteristic properties that differentiate the amyloid fibers from other fibrils; the β-strands-rich core lies at the heart of the amyloids uniqueness. The molecular patterns taken by that core are arranged in a plenty of 3D shapes which seem to be part of an ever-growing collection. That diversity in molecular structures revealed by different imaging techniques seems to reflect the multiple amino acid sequences associated with the globular proteins. The amyloid formation seems to be guided via specific pathways reflecting its protein amino acid sequencing and thus organizing the β-strands in various forms inside the amyloid core perpendicular to the fiber axis. Those repeated cross β-strands are typically arranged in-register forming β-sheets, where the stacking arrangement differs from one type of amyloid to another, and thus enables plenty of different substructures to evolve. Consequently, these different atomic substructures together with the aggregation pattern seem to determine the functionality/toxicity of the respective amyloids [64, 70].

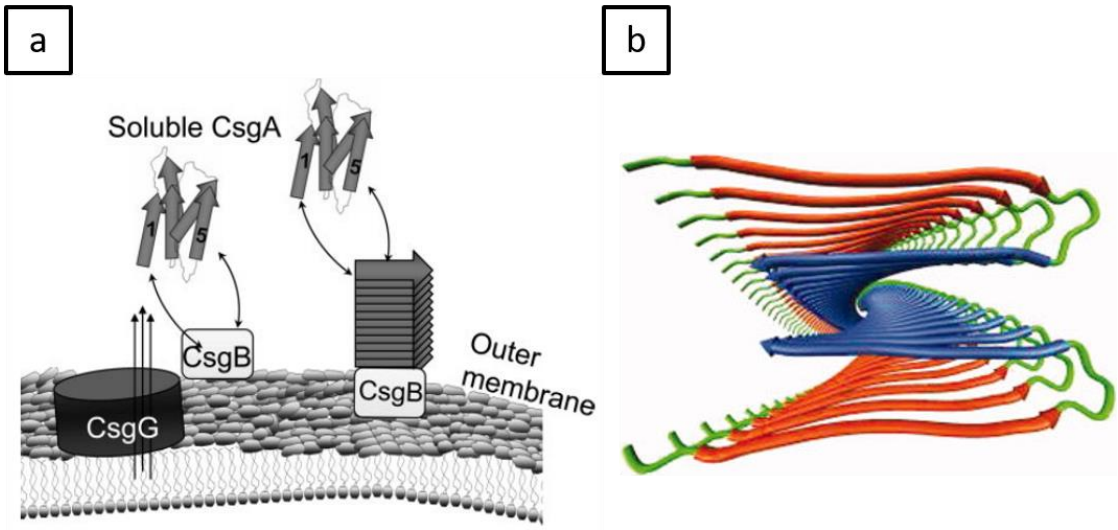

Figure 1.8 Biogenesis of amyloid nanofibers. (a) Amyloid formation at cell outer membrane [71]. (b) Molecular model of amyloid fibril twisted along the direction into the page (i.e. the fibril axis) [72].

Although the functionality of the amyloids was discovered recently, it is believed that it can be dated back to the pre-biotic world as, astonishingly, the first functional protein structure [73]. The functional amyloids were found to exist in plenty of organisms such as fungi, bacteria, and even mammals. Moreover, they are known to be very useful towards unraveling the details of the "amyloidogenesis" process with implications for the growth and toxicity of pathological amyloids [73-74].

In this thesis, we will be investigating the functional amyloid nanofibers secreted by *Escherichia coli (E. coli)*, which exhibit potential to be exploited as next generation dynamic biomaterials.

Curli fibers (or Curlins) are a compelling example of the *functional* amyloid nanofibers [75]. These bacterial fibrous proteins are extracellularly-secreted and classified as *adhesins* that aid *E. coli* bacteria to adhere to surfaces and assemble with other components, like cellulose, to form protective structures termed as *biofilms*. These biofilms offer a defensive shelter for large bacterial communities against harsh environmental conditions (e.g. extreme temperature, pressure, or pH) and also provide resistance against proteolysis, towards ensuring long-term survival. The curli fibers are regarded as the structural "spine" or "backbone" of these biofilm structures and play an

important role in determining overall mechanical properties. These curlins are synthesized by highly-controlled curli-specific genetic machinery which is encoded in the *E. coli* DNA by *csg* curli-responsible genes (i.e. csgDEFG and csgBA operons). The *csg* curli operons drive the expression of CsgD, CsgE, CsgF, and CsgG membrane secretory proteins which drives the extracellular secretion of the main precursors of the curli fibers: the minor subunit protein, CsgB, and the major subunit protein, CsgA. After these proteins (i.e. CsgA and CsgB) are secreted from the cell membranes, the polymerization (the fiber-assembly process) takes place on the outer-membrane of the cell [71, 76-77].

In this thesis, engineered genetic-mutants of *E. coli* are employed to extensively investigate functional amyloid nanofibers with different biochemical compositions via AFM imaging and nanoindentation experiments. The details of the experimental procedures and the obtained results are provided in the next chapters.

1.5 Outline

This thesis is divided into five separate chapters.

The current chapter (Chapter 1) presents an overview of the field of microscopy, specifically its history over the last few centuries. We briefly give an account on light microscopy, electron microscopy and the family of probe microscopy which the AFM belongs to. The STM (the predecessor of the AFM) is discussed in more detail by showing the improvements applied to it over years, as these improvements were directly transferred onto the AFM. AFM is introduced and several biological applications are listed. The chapter concludes by a brief intro to bacterial functional amyloid nanofibers.

Chapter 2 contains the underlying working principles associated with AFM imaging and force spectroscopy. Also, it presents a discussion of AFM calibration steps involving extracting the photodiode sensitivity (S) and the cantilever spring constant (k_{cant}) as well as the structural characterization of the tip apex via SEM. We conclude by briefly touching on the preparation of amyloid nanofibers for AFM experiments.

Chapter 3 includes an overview of practical procedures for AFM force spectroscopy. We discuss in detail the collection of the force-distance curves and their processing, which provides not only stiffness values associated with different amyloid nanofibers but also an estimation of the effect of the substrate on the measurements.

Chapter 4 presents the results of AFM experiments performed on 8 different amyloid samples in terms of morphological and mechanical properties (particularly, Young's moduli). We also discuss the rational tuning of mechanical stiffness and the use of a qualitative method to compare the morphological properties of the samples. We discuss the results in the context of being a function of biochemical composition, and we utilize statistical analysis to evaluate significant changes in measured properties.

Chapter 5 finally provides a summary of the thesis and an outlook regarding future directions of research.

Chapter 2

Experimental Methods

2.1 Imaging and Force Spectroscopy

As briefly described in Section 1.2.3, the atomic force microscope (AFM) is able to generate images with unpreceded spatial resolution down to the sub-nm scale, together with the detection of tip-sample forces down to the piconewton regime. The main constituents underlying AFM operation are carried out by several instrumental parts designed and installed to work together in harmony. These involve: (i) the cantilever with the sharp tip, (ii) the laser source, (iii) the position-sensing photodiode detector, (iv) the electronic feedback system, and (v) the piezoelectric actuators (as partially depicted in Figure 2.1).

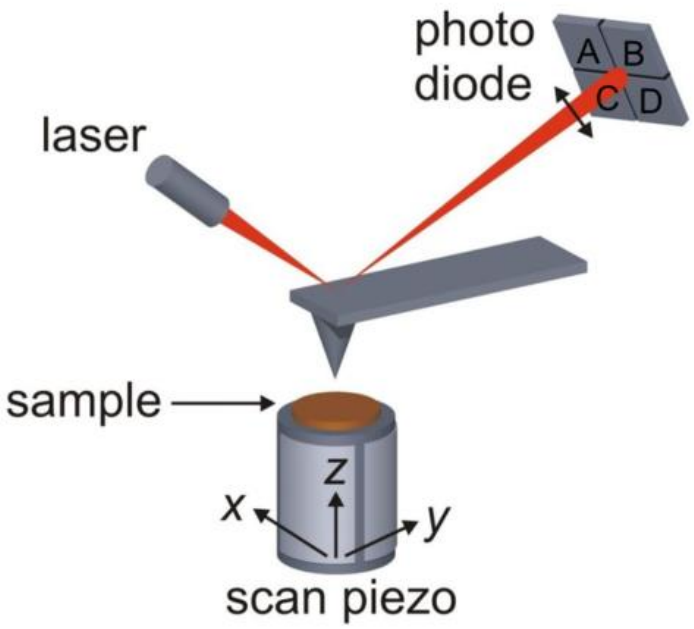

Figure 2.1 Simple schematic of AFM setup showing its basic operational principle [78].

A micro-manufactured cantilever, with a nm-scale-diameter sharp tip (or simply *probe*) located at its end (as revealed under SEM in Figure 2.2), transduces the repulsive as well as attractive interaction forces emerging between its probe and the surface when they come into contact, into deflections. These forces originating from "touching" sample features with the probe, deflect the cantilever in upward and downward directions while moving on the sample surface. To detect these deflections, an optical method is used, as explained below.

A laser beam directed to the topside of the cantilever, reflects onto a four-quadrant position-sensing photodiode (or simply PD). The cantilever deflections are monitored by changes in the position of the laser spot on the PD (see Figure 2.1 and Figure 2.3). The PD comprises four segments as seen in Figure 2.3 (first panel on the left), where each segment (A, B, C, or D) has its own voltage intensity. At the beginning of the experiment, the AFM operator should align the laser spot to be at the center of the PD as seen in Figure 2.3 (second panel). At the set-point, the voltage differences between either the upper and the lower quadrants ($(A + B) - (C + D)$) or the left and the right quadrants ($(A + C) - (B + D)$) are tuned to be *zero* before starting any measurements, as seen in Figure 2.3 (second panel).

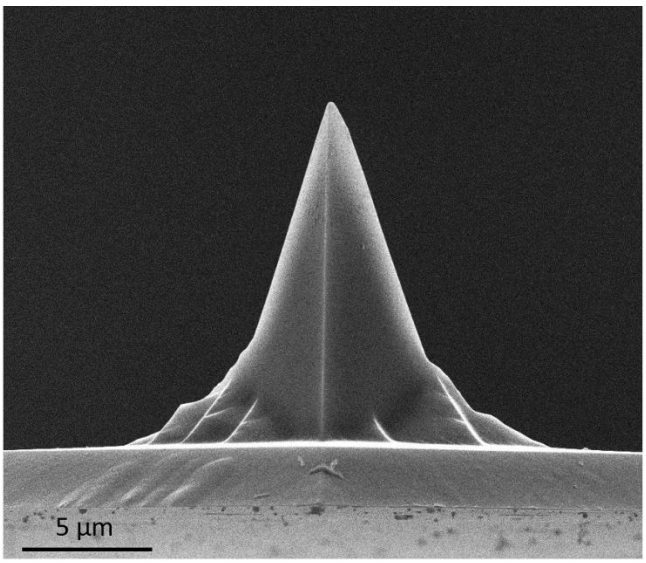

Figure 2.2 SEM image of the AFM cantilever tip used in this study.

During scanning, the "bumps and valleys" characterizing the surface topography of the sample cause the cantilever to deflect up or down in the vertical deflection, causing a change in the vertical position of the laser spot on the PD. For the sake of illustration, if a probe passed by a "bump" feature the cantilever would suffer an upward deflection that changes the optical beam path, whereby the laser spot on the PD will shift downwards as in Figure 2.3 (third panel). This downward shift can be precisely calculated from $(A + B) - (C + D)$ as a voltage difference (the voltage signals are converted to deflection values, in nm, as described in Section 2.2.1). In the same way, lateral forces due to friction between the tip and the surface would cause the cantilever to undergo torsional twisting and the laser spot would move horizontally, as shown in Figure 2.3 (last panel). While this is very useful for nanotribology experiments, in this thesis we will not be focusing on this aspect and therefore, the twisting of the cantilever should not be discussed in much further detail.

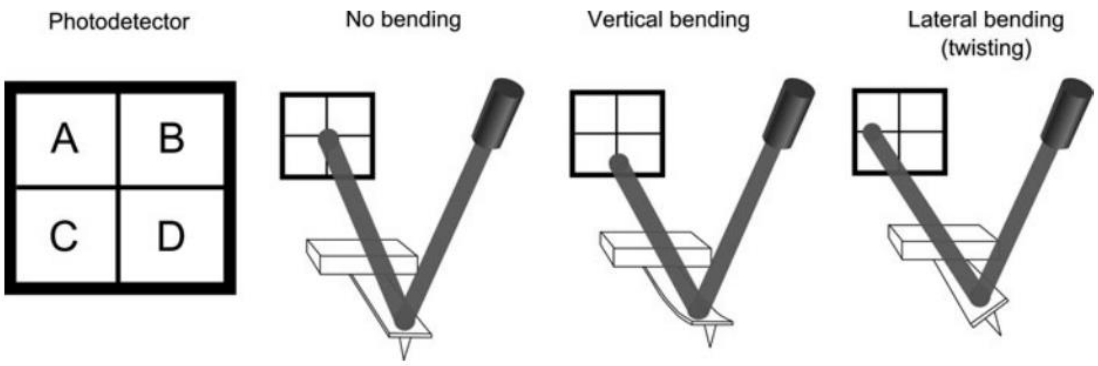

Figure 2.3 Photodiode scheme and laser spot position as a result of cantilever deflection [30].

After recording vertical voltage signals from the photodiode, they are sent to another part of the AFM setup, namely, the feedback controller, which takes the voltage signals from the photodiode and processes them to adjust the height of the cantilever over the sample surface in an appropriate way such that the deflection resets to a fixed set-point value during scanning. This height difference is recorded as the feature height at the point where the cantilever is deflected and topography maps are generated accordingly. For the sake of resetting the cantilever deflection to its set-point value, the piezoelectric z-scanner is actuated by the voltage signal from the feedback controller, and as such moves upwards/downwards to "relax" the cantilever and bring the deflection to its set-point value. To sum up, working together, the cantilever, the electronic feedback system and the piezoelectric scanner allow the probe to track effectively and accurately the topographical features on sample surface, as seen in Figure 2.4. Finally, by registering all movements of the piezoelectric scanner in the vertical *z* direction at all scanning points, 3D topographical images of complex sample surfaces can be generated as seen in Figure 2.5.

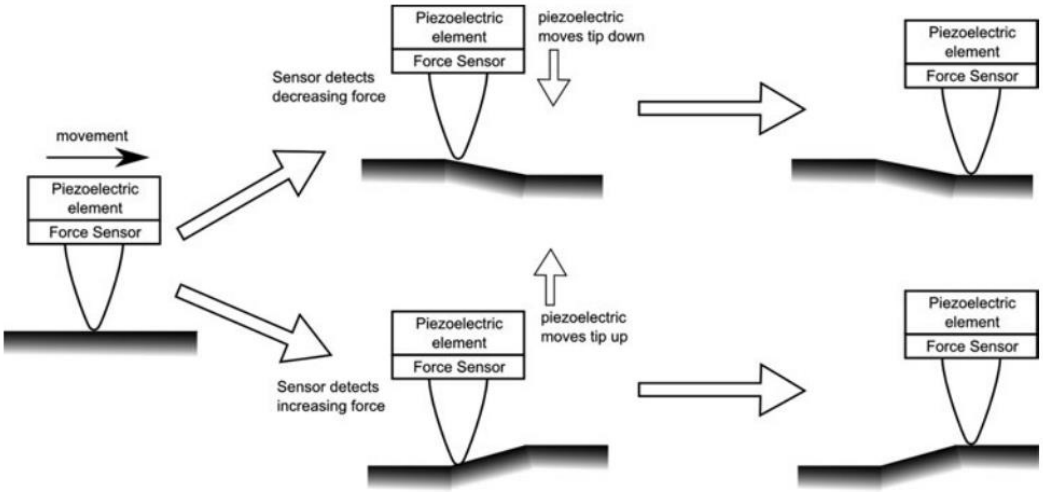

Figure 2.4 The AFM probe follows the sample topography in a smooth fashion as mediated by cantilever deflections, the respective vertical movement of the piezoelectric scanner and the control signals from feedback system [30].

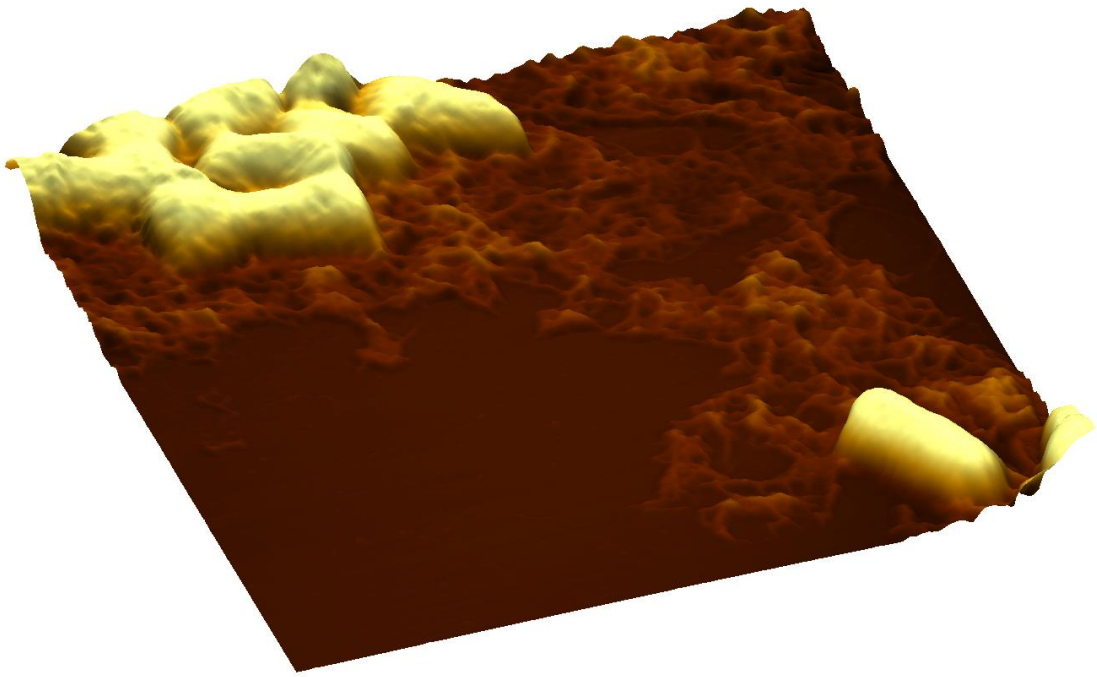

Figure 2.5 3D topography image of *E. coli* bacteria secreting networks of amyloid nanofibers to the extracellular environment, obtained by AFM. The image size is 9×9 μm^2 with a maximum height of ~200 nm [79].

When the tip never leaves the sample surface and is always in contact with the sample features while scanning, this AFM procedure (i.e. mode) is called *contact mode*. Although this is the most common AFM mode of operation, it is not the best fit for all samples, especially delicate ones that are weakly attached to their substrate. This issue is tackled by another AFM mode of operation called *tapping mode*.

Tapping mode involves excitation of the cantilever at its resonance frequency, causing oscillations. These oscillations are facilitated mainly by a piezoelectric element located at the cantilever holder driven by sinusoidal voltage signals. This mode not only cancels out any lateral "pushing" exerted by the AFM tip on weakly-attached specimens (as in contact mode), or preserve both the AFM probe and soft samples from wear and damage, but it also provides us with different channels of information about the sample. Precisely, the tip-sample interaction forces induce measurable changes in signals associated with cantilever oscillations such as: oscillation amplitude, frequency, and phase (sensitive to the sample composition). As in contact mode, any of these signals can be set to a reference value (i.e. "set-point") such that any variations induced by scanning the sample surface can be sent to the feedback controller as the input signal. Alternatively, these signals can be recorded to make conclusions about the physical properties of the sample. The oscillation amplitude is used mostly as the feedback signal during tapping mode AFM, whereby the feedback loop attempts to keep it constant during scanning, allowing topographical measurements based on changes in the tip-sample distance, as in contact mode imaging. The underlying working principle of imaging via tapping mode is described briefly in Figure 2.6.

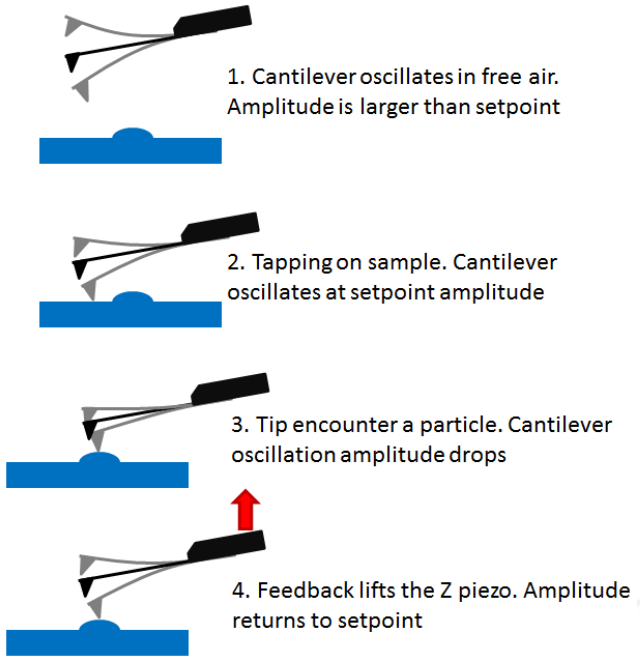

Figure 2.6 Basic principles of tapping mode AFM imaging [5].

"Feeling" the surface topography is not the only task that the AFM can perform. In particular, the capability of "pressing" into the surface is one of the main attractions that drove the scientists to use AFM extensively in studying several samples. Commonly termed as *force spectroscopy*, these experiment involve applying controlled deformations of the sample via the AFM tip by gradually "pressing" it into the surface, resulting in increasing interaction forces as reflected by larger cantilever deflections. The experiments typically result in the collection of *force vs. distance* plots (or simply, *FD curves*), as shown in Figure 2.7. Here, the tip-sample distance is controlled by the vertical displacement of the piezo scanner.

FD curves are classified into two types: approach and retractions curves. The approach curve in Figure 2.7 (starting with point A) comprises three main stages: At point A, the tip is away from sample surface and thus the cantilever is experiencing *zero* deflections (i.e. null forces), as expressed by the horizontal line. At B, while approaching the surface, attractive tip-sample forces *pull in* the AFM tip to the surface abruptly, as seen by the downward jump of the force to a minimum value, indicating downward deflections. Starting from B towards C, the cantilever is pressing (or indenting) into the sample via the tip apex and depending on the stiffness of sample surface, the rate of the

cantilever upward deflections (i.e. the slope of the line) will vary. Once the force reaches a pre-set maximum value, the retraction curve starts (i.e. the cantilever is pulled back from the surface). The D state resembles the retracting stage where the cantilever is moved up away from the surface. The attractive forces now delay the full detachment of AFM tip from the surface when compared to the pull-in stage during approach, as seen by the horizontal difference between the two dotted vertical lines. The force required to detach the tip from the sample surface (representing "adhesion") is also larger than the pull-in force, as reflected by a deeper minimum. Nevertheless, this thesis is concerned with approach curves that are used to extract the "stiffness" of the samples.

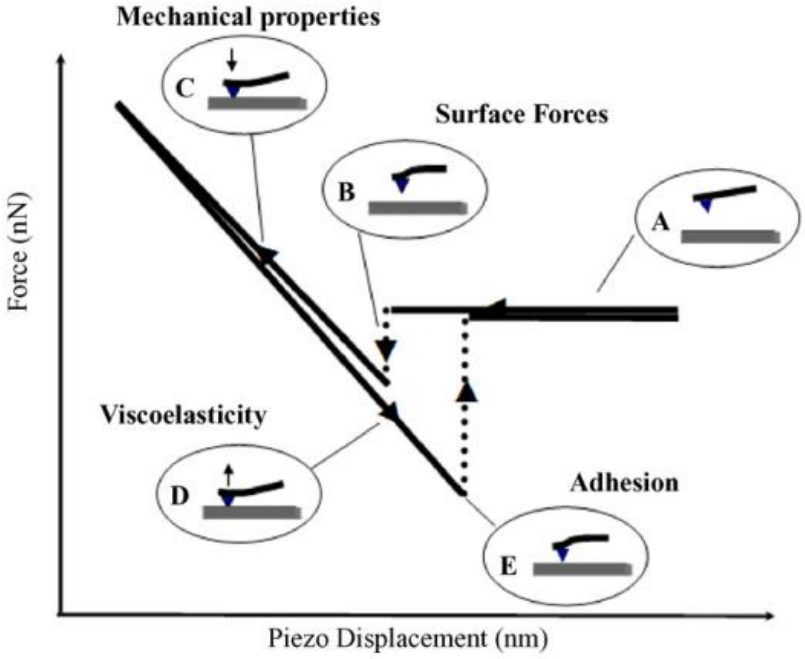

Figure 2.7 Schematic diagram of an FD curve with different stages of probe-surface interactions, via which various nanomechanical properties can be extracted [80].

The approach curves are characteristic to sample material in a way that collected curves from different materials most probably will exhibit differences in the associated slope values, indicating variations in nanoscale stiffness . For instance, the experimental FD curves shown in Figure 2.8 are acquired on genetically-different samples of amyloid nanofibers. The different slopes correspond to different mechanical stiffness; Highest slope corresponds to stiffest sample and lowest corresponds to softest sample (i.e. easily indented).

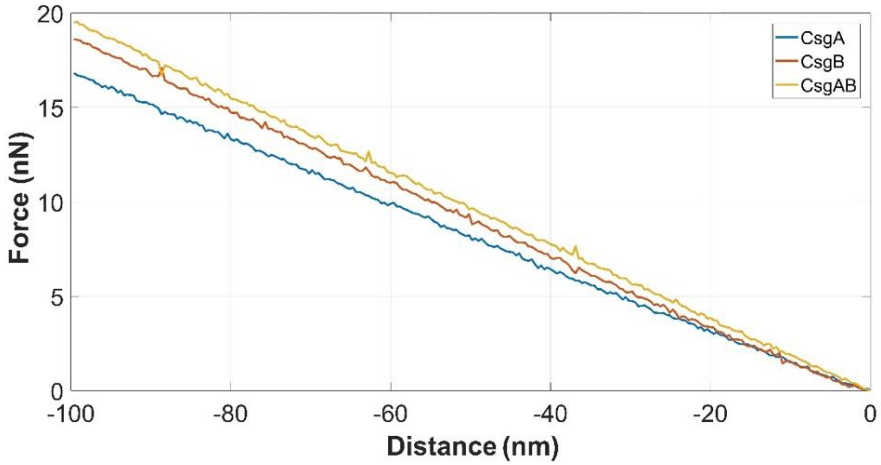

Figure 2.8 Representative FD curves extracted from force spectroscopy experiments performed on three different amyloid nanofiber samples (to be described later). Different slopes indicate different mechanical stiffness.

As we previously mentioned in this section, cantilever deflections are recorded as voltage differences (Volt) on photodiode segments and to convert these into force values (in Newton) at the tip-sample interface, photodiode sensitivity and cantilever spring constant parameters should be precisely determined.

2.2 Calibration Procedures for AFM

2.2.1 Photodiode Sensitivity Parameter (S)

The first step in AFM calibration procedures which is necessary to begin imaging and force spectroscopy measurements is the determination of the photodiode sensitivity parameter (S). The sensitivity parameter is in the very origin of cantilever deflection calculations, which are traced by an optical setup. This optical setup involves a laser beam re-directed by the cantilever back onto a four-segment photodiode (see Section 2.1). The vertical movements of the laser spot on the photodiode are accompanied by voltage differences that reflect the cantilever's upward and downward deflections. To transform these voltage variations on the photodiode (ΔV_{PD}, in Volts) to deflection values (d, in nm), the S parameter (of unit: nm/V) is needed. In that regard, the three values can be related to each other through the following equation:

$$d\ (nm) = S\ \Delta V_{PD} \tag{2.1}$$

In order to extract the S parameter experimentally, we perform force spectroscopy measurement (as described in Section 2.1) by acquiring FD curves on the mica subtsrate surface which is regarded to be "infinitely hard", and thus, exhibiting no indentation. As such, the entire downward movement of the *z*-piezo scanner (the piezo displacement, Z) is reflected in the cantilever deflection d (i.e. $d = Z$). Thus, the sensitivity parameter S can be extracted as the inverse of the slope belonging to each FD curve obtained on a mica surface (like the experimental curves shown in Figure 2.9).

To be more confident and precise in calculating the S parameter value, we collect several FD curves (~10) on the mica substrate per force spectroscopy experiment (as seen in Figure 2.9). We then take the largest S value (which is associated with the lowest indentation that resembles most closely the ideal condition of an infinitely hard surface) for carrying out deflection calculations. In our experiments, all extracted S values are centered around ~300 nm/V. This means when cantilever deflection reaches 300 nm, the laser optical path shifts the laser spot position on the PD such that a 1 V voltage difference is measured across it.

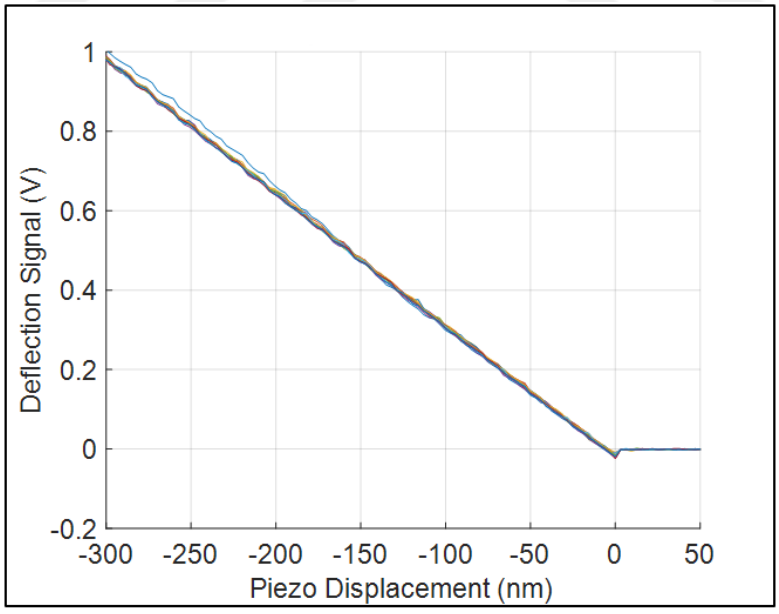

Figure 2.9 Photodiode sensitivity calibration. Several FD curves are taken on mica to extract the sensitivity parameter ***S***.

Because imaging more than one sample or imaging a single sample for a long time (~hours) can influence the $\boldsymbol{S}$ values and cause changes, we perform the related calibration step twice per sample to calculate $\boldsymbol{S_{before}}$, taken before the sample, and $\boldsymbol{S_{after}}$, taken after the sample. We choose only one of the two values to convert voltages to deflections per sample. This choice depends on when most of the nanoindentation experiments were carried out on the sample. If they were conducted towards the beginning of the measurements, we choose $\boldsymbol{S_{before}}$, otherwise we choose $\boldsymbol{S_{after}}$ as the final sensitivity parameter ($\boldsymbol{S_{final}}$). At the end, the $\boldsymbol{S_{final}}$ value is used to process the curves acquired from force spectroscopy experiments on a given sample and convert them from voltage vs. piezo displacement curves to deflection vs. piezo displacement curves. We list in the table below (Table 2.1) all the $\boldsymbol{S_{before}}$, $\boldsymbol{S_{after}}$, and $\boldsymbol{S_{final}}$ values that we have recorded for each sample of the amyloid nanofibers.

Table 2.1 Cantilever sensitivity parameters for all amyloid nanofibers.

Samples	$\boldsymbol{S_{before}}$ (nm/V)	$\boldsymbol{S_{after}}$(nm/V)	$\boldsymbol{S_{chosen}}$(nm/V)
CsgA	336.7	339.1	336.7
CsgB	339.1	334	334
CsgAB	334	344.6	334
CsgAM	330.7	310.1	310.1
CsgBM	310.1	339.6	310.1
CsgAM-BM	293.6	293.2	293.2
CsgAM-B	296.9	298.5	296.9
CsgA-BM	298.5	296.9	296.9

2.2.2 Spring Constant of the Cantilever ($\boldsymbol{k_{cant}}$)

High-resolution AFM imaging in contact mode and force spectroscopy via AFM requires the precise measurement of the normal forces acting on the AFM tip. In contact mode, the AFM instrument measures the cantilever deflection in the vertical direction (i.e. the *z*-direction) at each pixel of the image taken on the surface and then using the implemented electronic feedback mechanism in the AFM setup, the piezoelectric z-scanner (responsible for moving the cantilever base up and down) will adjust the height of the cantilever to keep the load applied by the tip to the sample surface (and thus the cantilever deflection) constant while imaging. This normal load (i.e. force) is calculated simply from Hooke's law, $F = k_{cant} * d$, where d is the cantilever

deflection, and k_{cant} is the cantilever spring constant which is a characteristic parameter for each cantilever.

Many methods in literature have been proposed to determine with precision the normal spring constant of AFM cantilevers but the method developed by Sader *et al.* is the most widely used by scientists due to its plainness, reliability, and robustness [81]. As such, it was used in this thesis to calibrate the single cantilever, used in all experiments, by finding its spring constant value (k_{cant}).

This method requires the knowledge of the resonance frequency of the cantilever, its geometrical dimensions, its mass and the density of the material it is made of. The reflective film of Aluminum (Al) used to direct effectively the laser spot towards the photodiode (PD) can affect the value of the cantilever spring constant and that is why this method accounts for it.

For a rectangular cantilever, the uncoated normal spring constant ($k_{uncoated}$) can be obtained as:

$$k_{uncoated} = M_e \, m \, \omega_{uncoated}^2 \tag{2.2}$$

where M_e is the normalized effective mass which relies on the aspect ratio of the cantilever (i.e. length/width); m is the uncoated cantilever mass; $\omega_{uncoated}$ is the angular resonance frequency of the "uncoated" cantilever in vacuum (2% of its measured value in air is added to account for the difference between the air-damped and the vacuum environments [81]). These parameters are as follows: M_e is taken as 0.2427 based on the length-to-width ratio (l/b); m is simply the product of the cantilever material density (that of Si) and its volume (provided by the manufacturer datasheet in terms of the cantilever dimensions); finally, $\omega_{uncoated}$ is known thanks to another equation that relates the angular frequency of the coated cantilever (ω_{coated}) which is typically measured by the AFM instrument software, to that of the uncoated one ($\omega_{uncoated}$) which is needed above for the k_{cant} calculation. This equation is [81]:

$$\frac{\omega_{uncoated}}{\omega_{coated}} = \sqrt{1 + \frac{\rho_{Al} \, h_{Al}}{\rho_{Cant} \, h_{Cant}}} \tag{2.3}$$

where ρ_{Cant} and h_{Cant} are the cantilever density and thickness, respectively, while ρ_{Al} and h_{Al} are their counterparts for the Al film coated on the back of the cantilever.

Finally, the spring constant of the coated cantilever (k_{coated}) can be related to that of the uncoated cantilever ($k_{uncoated}$) by the following equation [81]:

$$k_{coated} = k_{uncoated} \left(\frac{h_{Al}+h_{cant}}{h_{cant}}\right)^3 \frac{E_e}{E_{cant}} \tag{2.4}$$

where E_e represents the effective Young's modulus that accounts for both the elastic modulus of the cantilever material (Si) and that of the coating film (Al) which can be expressed by the equation below [81]:

$$E_e = \frac{E_{cant}h_{cant}+E_{Al}h_{Al}}{h_{cant}+h_{Al}} \tag{2.5}$$

Within the context of this method, the single AFM cantilever used in our experiments turned out to have an overall spring constant value (k_{coated}, or generally k_{cant}) of 0.20 N/m based on the data provided in Table 2.2, which lists the dimensional and material properties of the cantilever and its Al coating.

Table 2.2 Physical properties of the cantilever and its Al coating used in determining the spring constant of the cantilever.

$\boldsymbol{l}$ (μm)	450	$\boldsymbol{\omega_{uncoated}}$ (rad/s)	$\boldsymbol{2*\pi*f_{uncoated}}$
$\boldsymbol{b}$ (μm)	50	$\boldsymbol{f_{uncoated}}$ (Hz)	13,688
$\boldsymbol{h_{Cant}}$ (μm)	2	$\boldsymbol{h_{Al}}$ (nm)	30
$\boldsymbol{E_{cant}}$ (GPa)	130	$\boldsymbol{E_{Al}}$ (GPa)	70
$\boldsymbol{\rho_{Cant}}$ (g/cm^3)	2330	$\boldsymbol{\rho_{Al}}$ (g/cm^3)	2700

2.3 Tip Apex Characterization with SEM

A single probe (NanoSensors PPP-CONTR) has been utilized for all AFM measurements discussed in this thesis. The characterization of the tip apex by finding an estimate of its radius (R) is necessary for extracting accurate Young's modulus values from force spectroscopy experiments.

R can be estimated using scanning electron microscopy (SEM) imaging discussed previously in Section 1.1.2. Briefly, secondary electrons are used to obtain images of AFM tip apices as in Figure 2.10, such that extracting the R value is straightforward.

The SEM images shown in Figure 2.9 reveal a mostly blunt-ended tip apex which can be approximated structurally as a flat cylindrical punch with an equivalent radius of $R \approx 75$ nm. As shown in Section 3.1, this approximation aligns well with the acquisition of linear FD curves experimentally collected on the amyloid nanofibers, which is expected from the theory of Hertzian contact between an elastic flat-ended cylinder and an elastic, flat half-space.

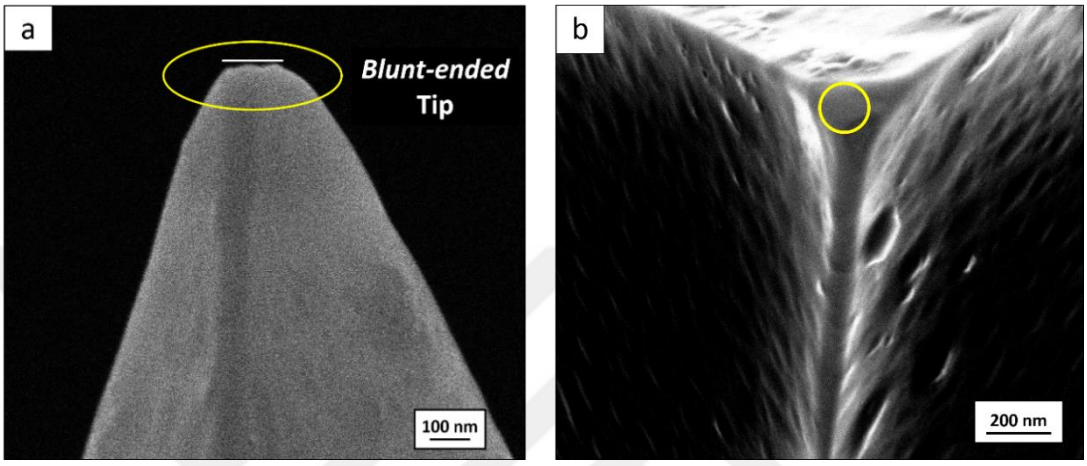

Figure 2.10 (a) Side-view and (b) top-view SEM images of the tip apex associated with the AFM cantilever used in the experiments [79]. The yellow circle in the top-view image has a radius of ~75 nm.

2.4 Sample Preparation

Now that the instrumental calibration has been discussed in detail, the chapter will conclude with a brief discussion of sample preparation procedures.

As we have discussed before in Section 1.4, in this thesis we are interested in the mechanical properties and morphology of amyloid nanofibers secreted by *E. coli* bacteria. CsgA and CsgB proteins constitute the genetic structure of these fibers where each one involves a different polymerization route (as shown in Figure 2.11 (a)). In order to explore their roles in the formation of the amyloid nanofibers, we used genetic engineering techniques to synthesize different versions of DNA vectors to express various amyloid nanofibers of different genetic origin. We used *E. coli* bacteria that lack both CsgA and CsgB as a platform to build the following DNA constructs: CsgA

alone (CsgB gene is knocked out), CsgB alone (CsgA is knocked out), and a DNA expression having both genes together (termed as CsgAB), where each genetic code is uploaded into different *E. coli* bacteria which are grown as separate populations. In addition to the already-mentioned three samples, we *modified* the genetic sequence of each protein by a histidine sequence (known as *his-tagging/linker-modification* process), and combined them in different ways to obtain five more samples in our collection, namely: CsgAM (CsgA protein is modified), CsgBM (CsgB protein is modified), CsgAM-BM (both proteins are modified), CsgAM-B, and CsgA-BM (only one of the proteins is modified). The samples are classified as follows: i) *Normal* samples (CsgA, CsgB, and CsgAB), ii) *Linker-modified* samples (CsgAM, CsgBM, and CsgAM-BM), and iii) *Complementary* samples (CsgAM-B, and CsgA-BM). All combinations induced the *E. coli* bacteria to secrete amyloid nanofibers into the extracellular matrix, which was validated under SEM prior to AFM imaging and force spectroscopy experiments as seen in Figure 2.11 (b). Finally, after being treated with appropriate antibiotics, chemicals and then incubated in their growth medium, the samples were drop-casted onto freshly-cleaved mica substrates and left to dry overnight under ambient conditions for subsequent AFM experiments.

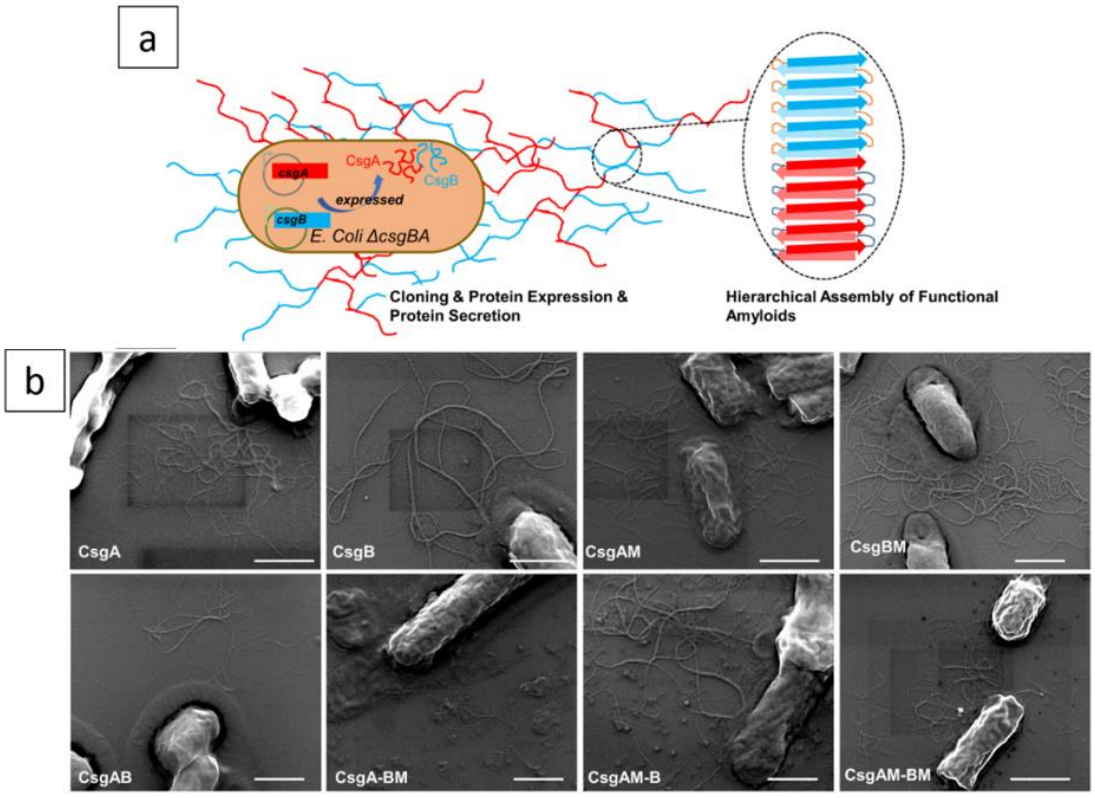

Figure 2.11 (a) Schematic representation of insertion of CsgA and CsgB genetic constructs into the *E. coli* DNA for protein expression. As a result, soluble CsgA and CsgB proteins are formed (expressed) inside the E. coli and secreted in the form of functional amyloid nanofibers into the extracellular environment constituting the backbone structure of the biofilm [79]. (b) SEM images of *E. coli* bacteria and secreted nanofibers. Scale bars are 1 μm.

Chapter 3

Data Acquisition and Analysis Procedures

3.1 Procedure for Force Spectroscopy Experiments

After recording a topography image on a representative region of a specific sample using contact mode AFM (as discussed in Section 2.1), several nanoindentation points are chosen manually on the amyloid nanofibers to guide the tip so that it indents at these points (as in Figure 3.1 (a)). Each nanoindentation point provides a single FD curve that reflects the changes in the interaction force between the tip and the sample as a function of piezo displacement (Figure 3.1 (b)). Each FD curve comprises two distinct parts: The first part shows negligible force interaction as the tip is away from the sample surface. The second part of the curve starts with the contact point (defined as ~ 0 nm piezo displacement) where the tip is pulled into the sample by attractive forces, followed by a diagonal-like line representing a linear increase in the interaction force as the piezo moves towards the sample surface, thus pressing the tip further into the sample.

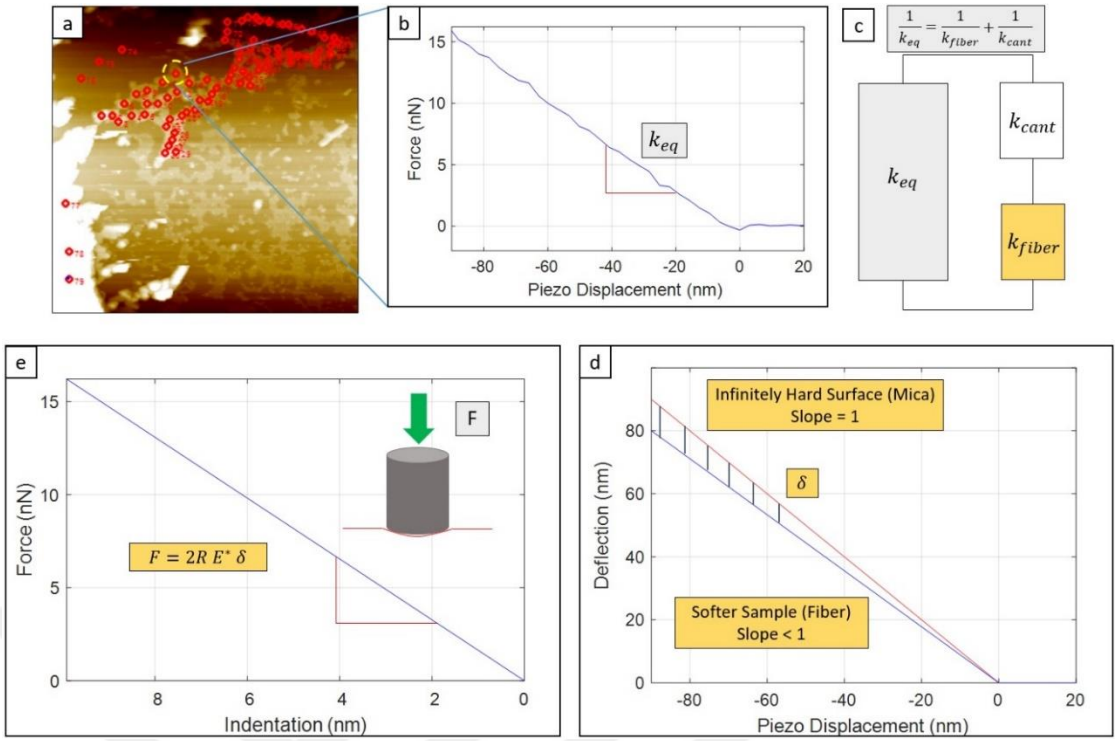

Figure 3.1 The procedure for the extraction of effective Young's moduli ($\boldsymbol{E^*}$) from the processing of FD curves. (a) AFM topography image taken on a region of the sample CsgAM-B, with red dots denoting the locations where the FD curves were collected. Several FD curves were taken on cells and mica for reference. (b) A single FD curve taken on the sample surface, showing linear increase of force with piezo displacement, where the slope is modeled as $\boldsymbol{k_{eq}}$. (c) The resistive spring model showing the relationship between the determined $\boldsymbol{k_{eq}}$ and both the cantilever spring constant ($\boldsymbol{k_{cant}}$). and that of the amyloid nanofibers ($\boldsymbol{k_{fiber}}$). (d) Two deflection vs. piezo displacement curves, corresponding to, respectively, (i) mica (taken as infinitely stiff sample, thus no indentation) and (ii) the amyloid fiber sample, used to calculate the indentation values ($\boldsymbol{\delta}$) at each piezo displacement. (e) The linear force vs. indentation curve extracted from the linear FD curve. The effective Young's modulus ($\boldsymbol{E^*}$) is determined from the equation in the inset which features the relation between interaction force and indentation values for the case of elastic Hertzian contact between a flat-ended punch and a flat half-space [79].

Extracting the final mechanical stiffness (i.e. the transversal Young's modulus) for a given sample involves several steps. It begins with extracting the slope of the second

part of FD curve and modeling it as the "equivalent" spring constant (k_{eq}). The k_{eq} value represents the "combined resistance to deformation" constituting (a) the cantilever resistance to upward deflections, lumped as the cantilever spring constant (k_{cant}) and (b) the deformation resistance of the amyloid fiber on which the FD curve is collected (modeled as k_{fiber}), as shown by the "springs in series" model in Figure 3.1 (c). k_{cant} is already estimated from the calibration stage described in Section 2.2 which makes the calculation of k_{fiber} very straightforward when k_{eq} is experimentally extracted. While k_{fiber} calculated for different samples can be used for contrasting of mechanical stiffness, it is not a universal unit of measurement for inherent material stiffness as it involves geometric effects. Therefore, we apply the steps described below to express the mechanical stiffness of each amyloid nanofiber sample in terms of a more *intrinsic* quantity, namely the Young's modulus, which provides a more suitable platform for comparisons with many other materials.

After extracting the k_{fiber} value from a given FD curve, two more curves are plotted to show how the cantilever "*deflection*" (which is related to the forces acting on the cantilever by Hooke's law, $F = k_{cant}\, d$) behaves with increasing magnitude of piezo displacement (Z): one is associated with the ideally stiff mica substrate (d_{mica} vs. Z) while the other is on the soft amyloid nanofiber (d_{fiber} vs. Z) shown as the red and the blue lines, respectively, plotted in Figure 3.1 (d). In the case of mica, the slope is 1 because the indentation into an infinitely stiff surface should be zero, i.e. all the piezo displacement towards the sample surface will be completely reflected in the cantilever deflection (hence, $d_{mica} = Z$). On the contrary, the amyloid curves always exhibit slopes smaller than 1 indicating that although the larger part of the piezo displacement will be converted into cantilever deflections, a small part of it will be consumed by the indentation into the fibers surface. This slope is equal to $\frac{k_{eq}}{k_{cant}}$ which is derived below.

On mica, the deflection-piezo displacement relation is:

$$d_{mica} = Z \tag{3.1}$$

Using simple Hooke's law, we can transform it to:

$$F_{mica} = k_{cant}\, d_{mica} \tag{3.2}$$

where F_{mica} is the force resulting from cantilever deflection on mica (in N). d_{mica} represents the cantilever deflection value on the mica substrate (in nm).

Plugging Equation (3.1) into (3.2), we have:

$$F_{mica} = k_{cant}\,\mathrm{Z} \tag{3.3}$$

Equation (3.2) can be written also for fibers as:

$$F_{fiber} = k_{cant}\,d_{fiber} \tag{3.4}$$

Recalling that any FD curve on amyloid nanofiber can be described as:

$$F_{fiber} = k_{eq}\,\mathrm{Z} \tag{3.5}$$

Thus, equating the right sides of Equations (3.4) and (3.5), we get:

$$d_{fiber} = \frac{k_{eq}}{k_{cant}} Z \tag{3.6}$$

which describes the deflection-piezo displacement ($d - Z$) relation due to amyloid nanofibers deformation, plotted in Figure 3.1(d). As mentioned before, its slope is always less than 1 because $k_{eq} < k_{cant}$.

In the next step, we use the two deflection curves described above to calculate the "*indentation*" values (δ) denoting the deformation depth into the amyloid nanofibers resulting from the tip's incremental pressing at each downward piezo displacement (Z). The δ values are calculated at each piezo displacement value from the following equation:

$$\delta = d_{mica} - d_{fiber} \tag{3.7}$$

which can be derived straightforwardly from Equation (3.1) in addition to the fact that piezo displacement (Z) is related to indentation and deflection values on amyloid nanofibers by:

$$Z = d_{fiber} + \delta \tag{3.8}$$

Then δ values are plotted against interaction force on fibers (F_{fiber}) calculated as in Equation (3.4) recorded at each piezo displacement value (Z) so that we obtain a "force vs. indentation" curve. Most of the literature performing force spectroscopy

measurements collect non-linear force-indentation curves but in our case, we observed a linear relationship between force and indentation for all investigated samples. This can be explained by the fact that the single tip used in our experiments exhibits a blunt-ended apex, as seen by SEM (Section 2.3), since Herztian contact theory expects linear force-indentation relationship between a flat-ended cylindrical indenter and an elastic half-space:

$$F = 2RE^{*}\delta \tag{3.9}$$

where R is the effective flat-punch radius estimated from the SEM image taken on the tip apex (Section 2.3) and $E^{*}$is the *effective* Young's modulus that still needs to be disentangled from the elastic modulus of the tip (E_{tip}), as well as the Poisson's ratio of the tip (υ_t) and the amyloid nanofibers (υ_f) as shown below:

$$E_{fiber} = \frac{1-\nu_f^2}{\frac{1}{E^{*}} - \frac{1-\nu_t^2}{E_t}} \tag{3.10}$$

The linear relationship between the interaction force on the fibers (F_{fiber} or simply, F) and the indentation (δ) can be derived based solely on Equations (3.1), (3.5), (3.6) and (3.7) as following:

$$\delta = d_{mica} - d_{fiber} = Z - \frac{k_{eq}}{k_{cant}}Z = \left(1 - \frac{k_{eq}}{k_{cant}}\right)Z$$
$$= \left(1 - \frac{k_{eq}}{k_{cant}}\right)\frac{F_{soft}}{k_{eq}} = \left(\frac{1}{k_{eq}} - \frac{1}{k_{cant}}\right)F_{soft} \tag{3.11}$$

Remembering that k_{eq}, k_{cant} and k_{fiber} are linked by the resistive spring model equation (Figure 3.1 (c)), the linear $F - \delta$ relation can be described for any linear FD curve simply as:

$$F = k_{fiber} * \delta \tag{3.12}$$

which means that E^{*}can be simply substituted in Equation (3.10) by:

$$E^{*} = \frac{k_{fiber}}{2R} \tag{3.9}$$

To study the deformation-dependent mechanical behavior along the depth of indentation through force spectroscopy experiments, each FD curve is divided into "segments" whose lengths are defined by the piezo-displacement values. Typically, each segment starts from the common zero piezo-displacement point and then starts to increase progressively by 1-nm steps till the segment length reaches 50 nm. Thus, we transform each FD curve into 50 segments (treated as 50 FD curves), all with the same starting point but with different lengths of 1 to 50 nm. The previously mentioned processing steps are repeated for each segment beginning from k_{eq} and ending with E_{fiber}.

To limit the contribution of the stiff substrate to the measured mechanical behavior of the fibers above, this procedure is stopped for any segment that results in indentations greater than or equal to 75% of the fiber height, so that the segments which result in indentation values exceeding the criterion will be discarded when determining the Young's modulus values. For each segment length, the mean and standard variation values of Young's modulus are calculated by considering all the FD curves collected on that sample region. In short, the scheme described before (that gives us E_{fiber} in the end) is carried out for each segment.

Finally, to evaluate the overall mechanical stiffness for a given sample, the mean and standard error of mean (SEM) of Young's modulus values is calculated by considering all segments (of lengths varying from 1 nm to 50 nm) that fulfill the <75% indentation criterion described above.

It should be mentioned that, to conduct force spectroscopy measurements, individual positions (i.e. red "dots" as seen in Figure 3.1 (a) and Figure 3.3) were chosen by hand onto which the tip moves and performs nanoindentation, after AFM imaging. The number of indentation points varies per sample type and imaged area. It depends mainly on how much of the images surface is covered by amyloid nanofibers.

"Thermal drift" can be considered as a common problem in AFM measurements such as ours that last over extended periods of time. This may cause the AFM tip to move away from the chosen nanoindentation points on the amyloid nanofibers and to be mistakenly positioned on mica or bacteria surfaces. To avoid considering any FD curve

that was taken by fault on mica/bacteria surfaces, several nanoindentation points are taken deliberately on mica and bacteria, together with the ones on amyloid nanofibers. The stiffness values deliberately acquired on mica and bacteria thus provide upper and lower limits between which amyloid nanofibers are expected to lie.

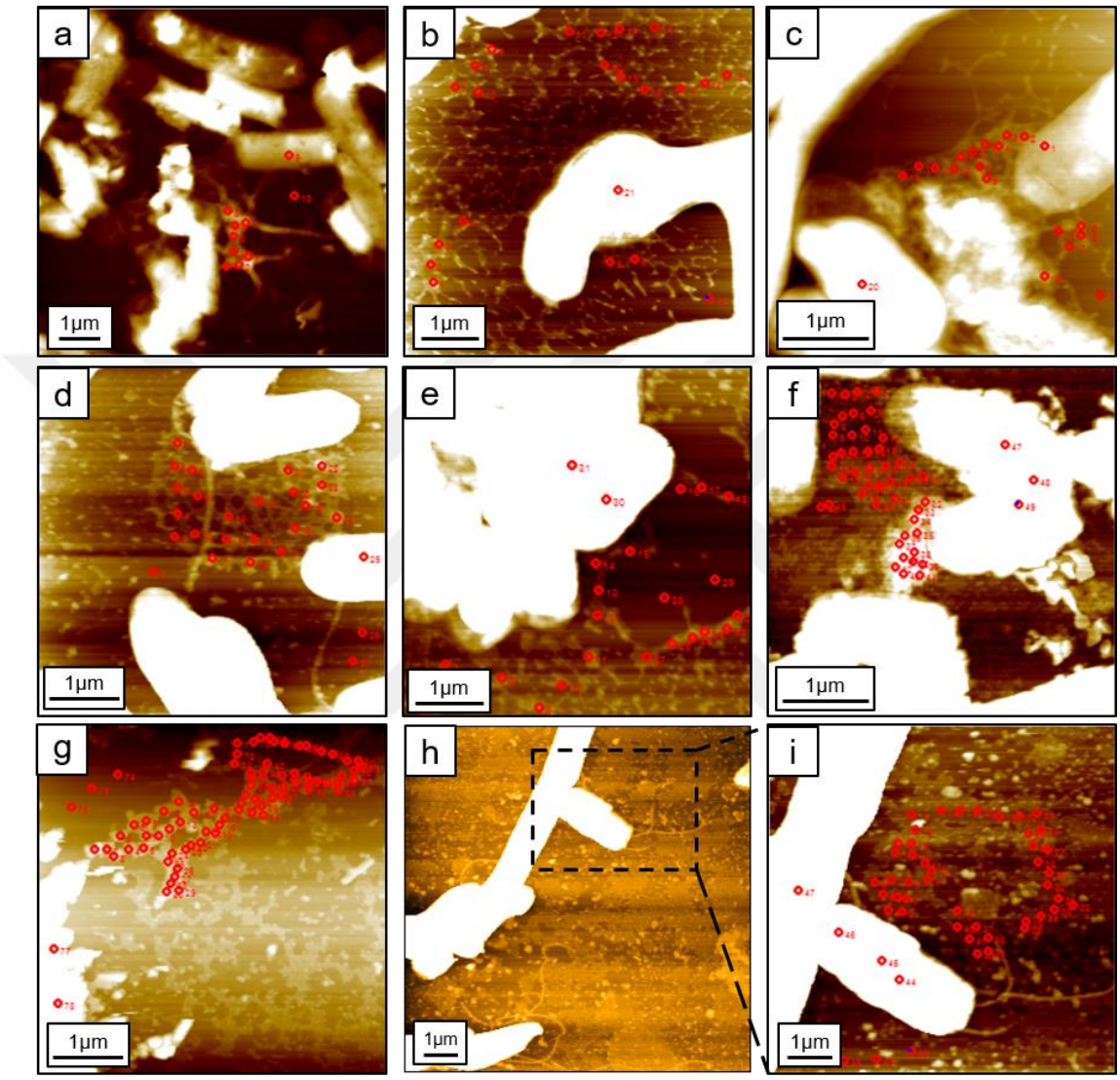

Figure 3.2 Various AFM images (taken in contact mode) with marked indentation points taken on different samples: (a) CsgA. (b) CsgB. (c) CsgAB. (d) CsgAM. (e) CsgBM. (f) CsgAM-BM. (g) CsgAM-B. (h) Zoomed-out view of CsgA-BM. (i) Zoomed-in view of CsgA-BM [79].

3.2 Effect of Substrate on Mechanical Stiffness

As it was outlined in the previous section, every FD curve contributes to the calculation of the overall Young's modulus values (mean and standard error of mean) in terms of its own "segments", where each segment represents a different piezo displacement (ranging from 1 to 50 nm separated by 1 nm steps) that correspond to different indentation depth into the sample surface. In that regard, having all the FD curves on a given sample region (like the ones in Figure 3.1 (a)), one can calculate and plot the mean and the SEM values for the overall Young's modulus as a function of the segment length, as shown in Figure 3.2. Using this plot, one can track the mechanical behavior change with increasing indentation into the sample. For example, in the plot below, one can observe two interesting behaviors: (a) the abrupt increase in Young's modulus until a segment length 9 nm, which can be attributed physically to a stiff shell encapsulating the soft amyloid core of nanofibers and (b) a gradual overall increase in Young's modulus with increasing segment length. The second observation can be attributed to the growing effect of the stiff mica substrate lying underneath the amyloid nanofibers on the measured stiffness with increasing segments lengths, and thus increasing indentations.

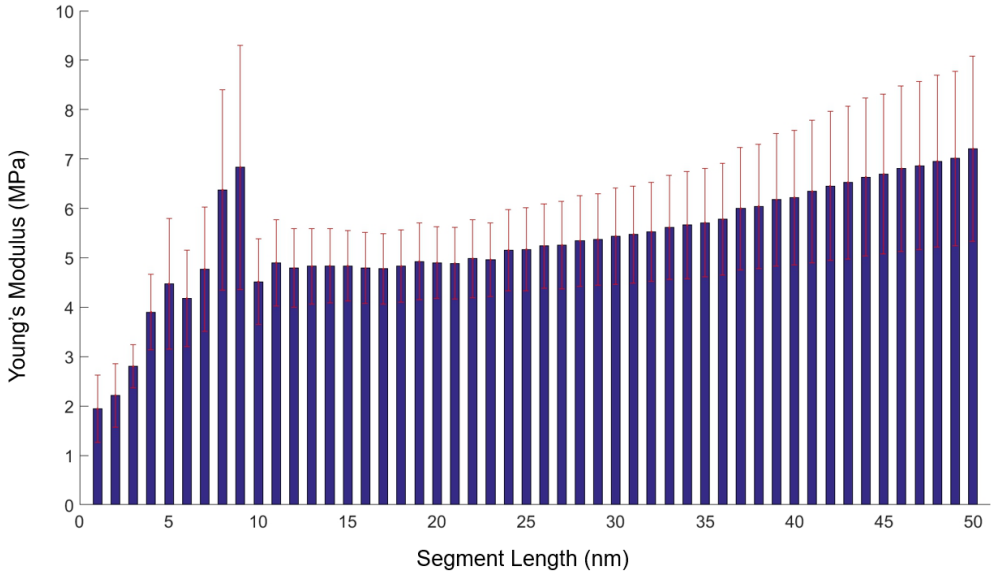

Figure 3.3 The variation of the mean Young's modulus values (blue bars) and the standard error of mean (SEM, red error lines) with segment length, recorded on the CsgA sample [79].

Chapter 4

Morphology and Mechanical Stiffness of Amyloid Nanofibers Measured by AFM

4.1 Morphology of Amyloid Nanofibers

In order to investigate the ability of tuning the morphological and mechanical properties of amyloid nanofibers constituting the backbone of bacterial biofilms, a comparative study has been postulated that includes three different groups of specimens. CsgA and CsgB proteins have different polymerization routes which give rise to different morphologies. We expect these morphologies induced by genetically-designed biochemical differences may lead a change in overall mechanical properties (specifically, Young's modulus) of amyloid nanofibers. For the sake of controlling by design the mechanical properties of secreted biofilm protein fibers, one needs to assess the mechanical properties of individual, isolated amyloids of CsgA and CsgB proteins, together with "modified" versions. The modification process is achieved via the use of genetic engineering methods to add histidine tags to the carboxyl end of CsgA and CsgB amino acid sequences. The Histidine tag is simply six repeats of the histidine amino acid. We analyze and quantify the morphology and mechanical behavior of CsgA and CsgB proteins as well as their mixture (CsgA-CsgB, or simply CsgAB) in addition to

the optional addition of histidine tags, which can be thought of as soft linker molecules. As mentioned before, the naturally-occurring biofilm structure comprises the genetic sequence of both CsgA and CsgB amyloid proteins, however in this thesis work, to control the overall mechanical properties of the fibers in terms of Young's modulus, we need to characterize them as individual isolated specimens. Consequently, this is achieved by generating various versions of amyloid nanofibers expressing standalone CsgA or CsgB proteins in addition to different mixtures of their native and "modified" versions. Precisely speaking, 8 different samples have been generated, which were classified into 3 different groups: *Normal* (CsgA, CsgB, and CsgAB), *Linker-modified* (CsgAM, CsgBM, and CsgAM-BM), and *Complementary* (CsgAM-B and CsgA-BM). The secretion of these amyloid nanofibers into the extracellular space has been validated by SEM as mentioned in the sample preparation section (Section 2.4), where we included the relevant SEM images (Figure 2.3 (b)).

The schematics presented in Figures 4.1, 4.2, and 4.3 show the basic hierarchical structure of functional amyloid nanofibers as expressed on the bacterial surface, involving alternative stacking of amyloid CsgA and/or CsgB β-sheets shown as blue and green *loop-strand-loop* models, respectively, as well as silver dots attached to the protein sheet (where applicable), denoting His-tagging. In order to characterize the morphology associated with the different types of amyloid fibers, three parameters are generally employed: (i) nanofiber size, (ii) tendency to form networks and if present, (iii) the lateral extent of these networks. The different samples can be compared in two ways: (i) the members of each group among themselves and (ii) the Normal and Linker-modified versions of the samples with each other.

Figure 4.1 portrays the structural morphology concerning the Normal group of samples: The CsgA sample (Figure 4.1 (d)) involves large-sized, thick nanofibers but not a tendency to form networks. Also, it should be mentioned that nanofibers were noticeably scarce and hard to find for this sample. On the other hand, the CsgB sample (Figure 4.1 (e)), despite exhibiting a much smaller fiber size, shows a clear ability to form porous networks around the bacteria, with noticeable lateral extent on the surface. Finally, the last sample in this group (CsgAB) exhibits the formation of thin amyloid nanofibers, with no tendency to form mesh-like networks (Figure 4.1 (f)).

As shown in Figure 4.2, for Linker-modified samples, the morphologies of the amyloid nanofibers are considerably different. The CsgAM sample exhibits small-sized nanofibers when compared to CsgA, but contrary to the normal sample, it shows also the ability to connect fibers in the form of a mesh-like network around the bacteria, although to a relatively short lateral extent (Figure 4.2 (d)). The high-resolution AFM image of CsgBM (Figure 4.2 (e)), on the other hand, shows a relatively large number of small-sized nanofibers dispersed on the surface, but without the ability to form any mesh-like network. Interestingly, the CsgAM-BM sample results in a continuous biofilm-like structure composed of small-sized fibers with a heterogeneous distribution of thickness on the substrate (Figure 4.2 (f)).

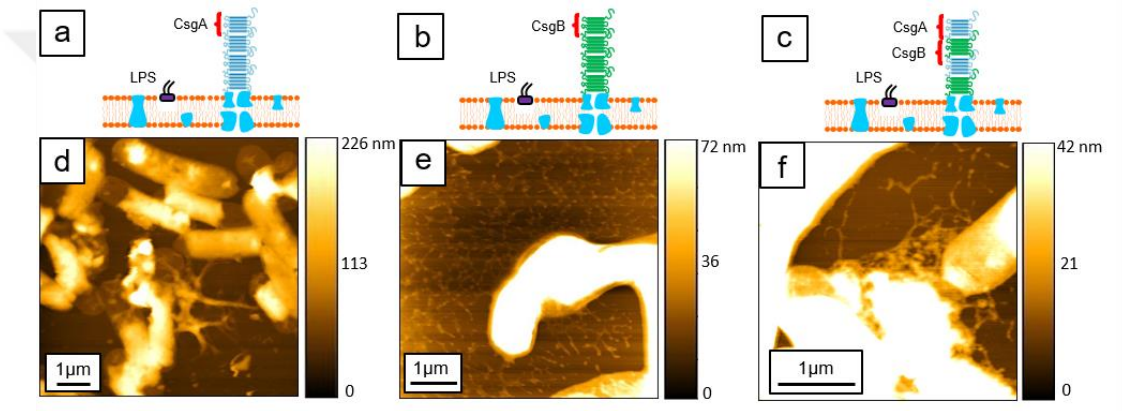

Figure 4.1 Morphological images of the Normal group of samples as probed by AFM. Structural schematics which correspond to samples CsgA, CsgB, and CsgAB are shown in (a), (b) and (c), respectively. Topography images taken on each sample together with their scale bars are shown in (d), (e), and (f) [79].

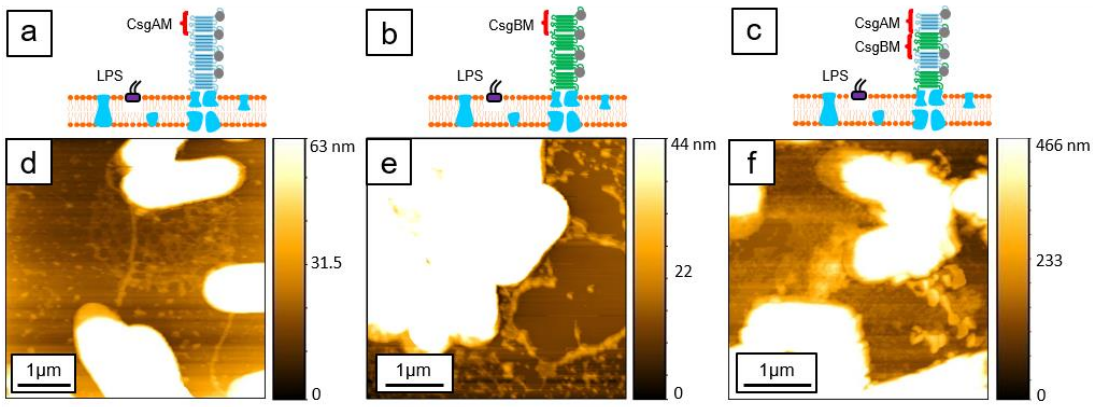

Figure 4.2 Morphological images of the Linker-modified group of samples as probed by AFM. Structural schematics which correspond to samples CsgAM, CsgBM, and CsgAM-BM are shown in (a), (b) and (c), respectively. Topography images taken on each sample together with their scale bars are shown in (d), (e), and (f) [79].

Lastly, Figure 4.3 presents the morphology of the samples in the Complementary group, where only one of the two proteins (CsgA or CsgB) is "modified". As one can see in Figure 4.3 (c), the CsgAM-B sample features chain-like amyloid nanofibers bursting out of bacteria edges forming large-extent porous networks, which exhibit larger void regions in-between when compared to the CsgAM-BM case. On the other hand, the CsgA-BM sample, shown in Figure 4.3 (d), features a remarkable formation of a much more homogenous, long-range, sheet-like structure consisting of fibers merged in a film-like manner and extending all around bacteria.

It is to be noted that the mean values of the nanofiber height for each sample were determined as follows: CsgA (60 nm), CsgB (13.5 nm), CsgAB (9 nm), CsgAM (5 nm), CsgBM (12.5 nm), CsgAM-BM (17.5 nm), CsgAM-B (12.5 nm), and CsgA-BM (7.5 nm). On the other hand, no significant correlation between different types of samples and associated heights has been found in the context of expected fiber structure.

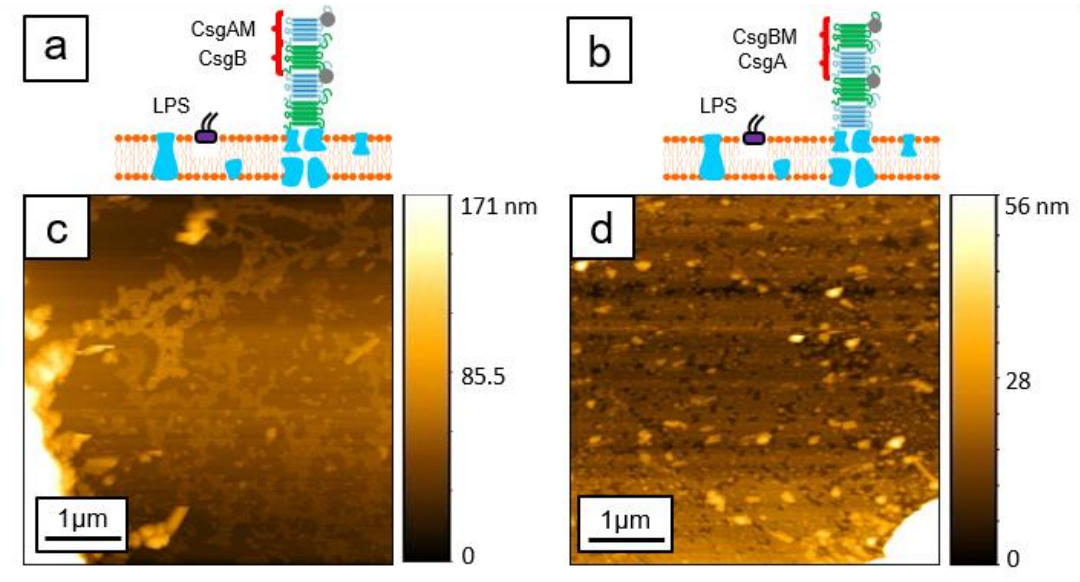

Figure 4.3 Morphological images of the Complementary group of samples as probed by AFM. Structural schematics which correspond to samples CsgAM-B, and CsgA-BM are shown in (a), and (b), respectively. Topography images taken on each sample together with their scale bars are shown in (c) and (d) [79].

As a way of interpreting the mesh-like network forming capability (or simply, the "meshing" ability) of the amyloid nanofibers in each sample, we devised a simple methodology. The ability of a given sample to form mesh-like networks is denoted in the following fashion: A "+" sign indicates that the sample does form mesh-like networks and a "-" sign indicates that it doesn't. The methodology additionally involves "+" and "-" signs assigned to the factors that are observed to affect the meshing ability of the sample, namely: (i) the "modification process" and (ii) the "combination process" of the CsgA and CsgB proteins (in their Normal or Modified states). First, for cases where CsgA and CsgB proteins are secreted individually, modification is observed to invert the meshing ability (as deduced by a comparison of morphologies in Figure 4.1 (d,e) and Figure 4.2 (d,e)) and thus assumes a "-" sign. Additionally, the process of combining CsgA and CsgB proteins to obtain CsgAB is seen to result in a sample with no meshing ability; the combinations process is thus assigned a "-" sign, as well. The final ability of a given sample to form mesh-like networks can be eventually determined by the mesh-forming ability of the initial state of the sample, and/or the existence of modification and combination factors of "-", as summarized in Table 4.1.

For instance, while the CsgA (CsgB) sample initially does not possess (possesses) the meshing ability and thus starts with a "-" ("+") sign, modification results in the multiplication of the original state by a "-" sign and thus, the inversion of the meshing ability for CsgAM (CsgBM). Since there are no "initial states" for samples that involve protein combinations, the meshing ability is determined by the existence or absence of modification and combination processes. In particular, CsgAB does not exhibit any meshing ability, as it is the result of protein combination only. On the other hand, all samples that involve the combination of two proteins out of which at least one is modified do demonstrate the meshing ability (reflected by the multiplication of two "-" signs: one due to the "modification" factor, the other due to the "combination" factor).

Table 4.1 Summary of the meshing ability for all investigated samples, as influenced by the His-tagging and combination processes.

Sample	Combination and Modification Factors	Meshing Ability (+/-)
CsgA	---	(-)
CsgB	---	(+)
CsgAM	(CsgA: -)*(-)	(+)
CsgBM	(CsgB: +)*(-)	(-)
CsgAB	(-)	(-)
CsgAM-BM	(-)*(-)	(+)
CsgAM-B	(-)*(-)	(+)
CsgA-BM	(-)*(-)	(+)

4.2 Mechanical Stiffness of Amyloid Nanofibers

Subsequent to the investigation of the morphological properties associated with amyloid nanofibers via AFM imaging, as described in the previous section, numerous FD spectroscopy experiments (known as nanoindentation process) have been conducted on

each of the investigated samples to extract mean Young's modulus (E_{mean}) and standard error of the mean (SEM) values (for details of the measurement procedure please see Section 3.1). Several indentation points were chosen on amyloid nanofibers as demonstrated before in Section 3.1 to ensure that measurements are statistically satisfactory per sample. The experimental procedure to collect, process, and extract Young's modulus values for fibers were explained in detail in the previous chapter (Chapter 3).

The results of these experiments can be summarized in Table 4.2 and Figure 4.4. Figure 4.4 (a) was extracted using two-way ANOVA comparisons of CsgA, CsgAM, CsgB, CsgBM and CsgAB samples. Figure 4.4 (b) was prepared using one-way ANOVA comparisons of CsgAB, CsgAM-B, CsgA-BM and CsgAM-BM samples. The ANOVA comparison is a statistical method to determine if there is a "significant" difference between two or more groups of samples based on the results of mean and standard variations, as well as the number of measurements taken.

The values reported in Table 4.2 and Figure 4.4 direct us to infer that the rational tuning of the mechanical properties of the amyloid nanofibers in terms of its transversal stiffness (as assessed by the overall sample mean value, E_{mean}) can be achieved via genetic engineering. The first 4 samples located in Table 4.2 constitute the rest of the samples. They are the stand-alone CsgA and CsgB proteins in their normal and Linker-modified versions (CsgA, CsgB, CsgAM and CsgBM) which give rise to the remaining samples (i.e. CsgAB, CsgAM-BM, CsgAM-B and CsgA-BM) which are essentially the resultants of combinations involving the first four samples. One of the most important comments that can be made based on these results is that each resultant sample of protein construct formed from a combination of two elementary proteins shows a Young's modulus value that exceeds the individual Young's modulus values of its constituents. For example, the E_{mean} value for CsgAB (11.6 MPa) is larger than that of both CsgA (9.5 MPa) and CsgB (10.0 MPa). Similar results occur case CsgAM-BM (14.8 MPa vs. 8.4 MPa and 13.9 MPa), and again for CsgAM-B (10.4 MPa vs. 8.4 MPa and 10.0 MPa) and most significantly, for CsgA-BM (18.9 MPa vs. 9.5 MPa and 13.9 MPa), showing clear evidence that mechanically stiffer amyloid nanofibers can be deliberately obtained by combining the secretion of major and minor proteins' native and Linker-modified versions.

Table 4.2 Young's modulus (mean and standard error of mean) values for all samples classified in the Normal, Linker-modified and Complementary groups [79].

Amyloid Nanofiber Samples	E_{mean} (MPa)	SEM (MPa)
CsgA	9.5	1.4
CsgB	10.0	0.7
CsgAM	8.4	0.8
CsgBM	13.9	0.8
CsgAB	11.6	0.8
CsgAM-BM	14.8	0.8
CsgAM-B	10.4	0.6
CsgA-BM	18.9	1.0

Additionally, we interestingly found that the Normal group of samples reveal a slightly increasing trend in the mean values of Young's modulus when advancing from CsgA, to CsgB, and finally to CsgAB. This monotonic tendency in the mean Young's modulus values is observed to be again sustained in the case of Linker-modified versions of the samples (CsgAM, CsgBM, and CsgAM-BM). In addition to all preliminary observations that were put forward in this section concerning mechanical properties, the statistical significance of the correlated differences in Young's modulus values between the samples needs to be interpreted in detail, as discussed in Section 4.3 and Figure 4.4.

The analysis of AFM force spectroscopy experiments presented until now unveiled that the mechanical stiffness of the amyloid nanofibers constituting the backbone of bacterial biofilms can be rationally tuned via genetic engineering, by the controlled secretion of amyloid backbone proteins CsgA and CsgB, together with their Linker-modified versions. A discussion of the related observations is presented in Section 4.3.

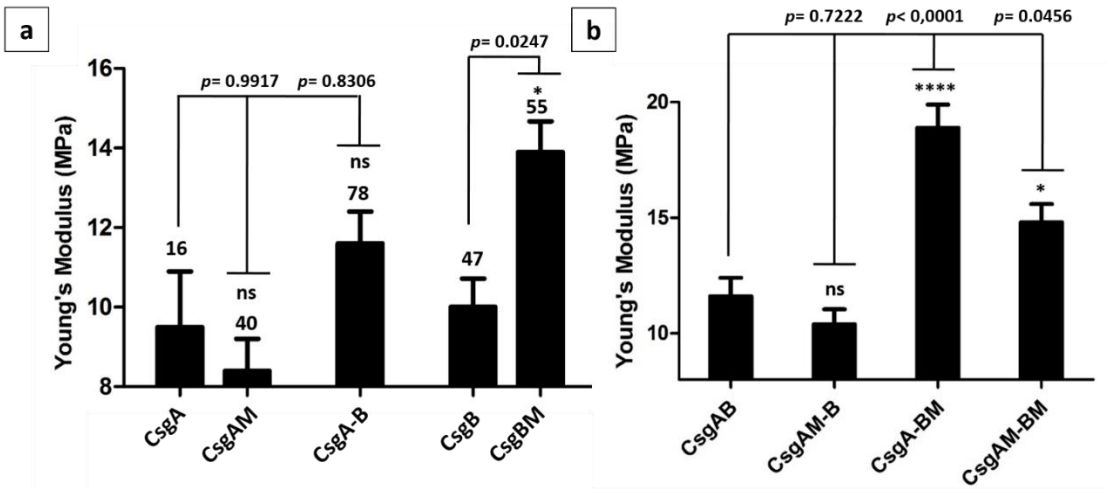

Figure 4.4 Young's modulus values associated with major and minor proteins as well as their Linker-modified versions, along with statistical analysis. Error bars represent SEM (standard error of mean). (a) Two-way ANOVA comparison shows that Linker-modification significantly causes an increase in the Young's modulus value of the minor protein (CsgB) but not the major protein (CsgA). Repeat numbers of Young's modulus experiments conducted for each sample are written above the respective column. (b) One-way ANOVA comparison underlines the significance of the modification of the minor protein, in contrast to the so-called major protein, with respect to its role in increasing the Young's moduli of amyloid nanofibers that it is a part of (ns: not significant, *: significant, ****: extremely significant, $p < 0.05$) [79].

4.3 Discussion of Results

As established above, it appears that the mechanical properties of engineered biofilm backbones can be deliberately tuned by controlling the genetic expression and modification of CsgA and CsgB proteins individually. This also fits well with previous observations arguing that the secretion of CsgA and CsgB proteins individually induce certain morphological changes of biofilm structures according to amyloid-dye-binding staining results [77]. Nevertheless, as shown in Figure 4.4 (a), we observed that results from the Normal group of samples show no significant difference between each other in terms of mechanical properties. Moreover, the Young's modulus values of CsgA and CsgB nanofibers are roughly the same which is not strange due to their high sequence

analogy. These two proteins have similar self-assembly mechanisms which can be the underlying reasoning for their homologous structural features as discussed previously. As morphological features of the amyloid nanofibers are expected to influence their mechanical properties, it is no surprise that force spectroscopy measurements revealed that the Young's modulus values of CsgA and CsgB are more or less similar. In alignment, the statistical analysis displayed an insignificant change in the mechanical stiffness of CsgA when combined genetically with CsgB to form the native biofilm backbone structure (CsgAB), as seen in Figure 4.4 (a).

Subsequent to these results and for a more complete study, we genetically modified the CsgA protein, as explained before, to obtain CsgAM. This has triggered no significant change in the Young's modulus value (Figure 4.4 (a)). On the other hand, modifying the CsgB protein (and thus, obtaining CsgBM) stimulated a statistically significant increase in the Young's modulus, thus putting forward the idea that the modified CsgB protein could dominate the controlled variations of the Young's modulus of the biofilm backbone formed by genetically-engineered amyloid nanofibers (Figure 4.4 (a)). To examine this hypothesis, we made comparisons between CsgAB amyloids and the complementary samples (CsgAM-B and CsgA-BM). The histograms given in Figure 4.4 (b) show that exchanging the CsgA protein with its modified version CsgAM in the CsgAB genetic construct does not have any significant effect on the mechanical properties of the final nanofiber structure (CsgAM-B), which aligns well with our previous comparison of single-protein fibers: CsgA vs. CsgAM. Swapping CsgB with its Linker-modified version CsgBM, on the other hand, triggers a dramatic increase in the Young's Modulus of the resulting CsgA-BM amyloid backbone, which was found to be, statistically speaking, "extremely significant" (denoted by " **** " above the column associated with the CsgA-BM sample). Furthermore, combining CsgAM along with CsgBM in one amyloid genetic sequence led to an increase of the Young's modulus value of the final nanofiber structure (CsgAM-BM) when contrasted with the native backbone fibers (CsgAB). While this increase is statistically significant, the Young's modulus of the CsgAM-BM nanofibers is smaller when compared to that of the stiffest backbone of all samples, CsgA-BM. Moreover, it can be observed from the data listed in Table 4.2 or shown in Figure 4.4, that samples involving CsgBM result in higher Young's moduli when compared to their counterparts involving the native CsgB. For

instance, amyloid nanofibers formed by the CsgA-BM protein construct are stiffer than those formed by CsgAB (18.9 MPa vs. 11.6 MPa) and nanofiber structures secreted by CsgAM-BM bacteria are stiffer than those formed by CsgAM-B (14.8 MPa vs. 10.4 MPa). These results and analysis suggest that the Linker-modified CsgB protein (CsgBM) plays a key role in controlling the mechanical properties of genetically-engineered amyloid nanofiber structures.

Studies in the literature show that CsgB is essential for the biogenesis of the *E. coli* biofilm as it plays a crucial role as seeding molecule and scaffold for CsgA self-polymerizing to form hierarchically self-assembled amyloid fibers, a process known as self-nucleation [82-83]. Our findings reveal that the genetic engineering of the CsgB protein sequence via *His-tagging/Linker-modification* can be used as a significant tuning element to control the mechanical properties of the resultant biofilm structures. Additionally, it can be observed via Figure 4.2 (e) that amyloid structures formed by CsgBM alone could not form largely-spread continuous biofilm backbone networks with high homogeneity. As such, there is a need for CsgA protein to be exploited (in its normal or linker-modified states) together with CsgBM to develop robust biofilm morphologies with low porosity as in Figure 4.2 (f) and Figure 4.3 (d).

While evaluating and discussing our results in the context of other studies in the literature, it is very crucial to put forward the potential physical reasons underlying the observation of MPa-range Young's moduli values for the amyloid nanofibers presented in this thesis. It is now established in literature that aggregation configuration of amyloids seems to be widely accessible by different kinds of peptides where elastic properties seem to be governed by intermolecular forces that dominate and define the assembly pathways [84]. In that regard, a wide range of Young's modulus values can be expected for different amyloid materials. In particular, we reported here values that fit very well with several other works in the literature [44, 84-85]. On the other hand, there are other reports in the literature that revealed, interestingly, Young's moduli in the GPa-range for other proteinaceous amyloid fibers, conducted via various force spectroscopy techniques [75, 86-89]. Therefore, starting from the fact that morphological property variations are accompanied by significant differences in mechanical stiffness values as presented in this thesis, structural features can be generally expected to play a critical role in the observation of such a wide span in the

values of Young's moduli of amyloid materials, covering MPa and GPa ranges. Interestingly, we observed that the amyloids exhibiting Young's modulus values in the GPa-range in the literature seem to exist as mostly straight, defect-free, and individual tubular structures of defined diameters, or packed in certain geometries along their axial contours [75, 86-89]. These morphological characteristics seem to be absent in the studies reporting Young's modulus values in MPa-range: The amyloid fibers with Young's modulus values in the MPa-range self-assemble into much more irregular, zig-zagged and branching structures [44, 84-85]. The influence of these subtle structural features as variations in measured mechanical stiffness is manifested clearly in two separate reports in literature investigating insulin amyloid fibers which demonstrated significantly different values for Young's modulus (5-50 MPa vs. ~3 GPa), whereby the fibers showing more irregular patterns exhibit the smaller Young's modulus values [44, 75]. Consequently, when we take into account our highly-branched and morphologically irregular structures synthesized from functional amyloid fibers secreted by E. coli bacteria as presented in thesis, the observation of Young's modulus values falling in the MPa-range is not surprising. Finally, as previously mentioned in the literature, the additional geometric constraints necessary for packing amyloid fibers of large length in a stable fashion may lead to disruption of the whole amyloid structure, facilitating preferential fractures to exist and thus giving rise to branched/aggregated fiber morphologies [84]. These assemblies would be expected to exhibit mechanical weakening in return for the ability to cover/colonize larger surface areas via branching and aggregation configurations.

Chapter 5

Summary and Outlook

The work presented in this M.S. thesis covers AFM contact-mode imaging and force spectroscopy experiments performed on bacterial functional amyloid nanofibers under ambient conditions. Special emphasis has been placed on the determination of mechanical stiffness variations induced by genetic engineering. Remarkably, the results underline that genetic engineering can lead to the rational tuning of mechanical stiffness as well as morphological properties, paving the way for bacterial functional amyloid nanofibers as strong candidates for next generation biomaterials.

Self-assembled biofilm structures help bacterial communities in colonizing surfaces and in surviving over extended periods of time under extreme conditions. Bacterial functional amyloid nanofibers constitute the "backbone" of the biofilms produced by *E. coli* bacteria. The nanofibers comprise CsgA and CsgB proteins. These functional amyloids are highly-organized, protein-based nanostructures which can be, in principle, re-programmed to serve in applications at the nano-bio interface. For instance, nanomaterial templating and self-growth was shown to be a direct application of nanofiber-forming capacity of bacterial biofilms [90-91]. Protein-based nanostructures are promising candidates to be used as genetically-expressed components in hybrid self-assembled material systems [92]. As such, the native polymerization routes in bacteria can be used in synthetic biogenesis to hybridize protein-based nanostructures

of different origins [93]. Nevertheless, lack of knowledge regarding the effect of biochemical changes on the nanoscale morphological and mechanical properties of bacterial functional amyloid nanofibers mostly prevent them from fulfilling their potential in full.

Motivated as above, we present in this thesis an extensive study involving contact-mode AFM imaging and nanoindentation experiments performed on bacterial functional amyloid nanofibers, secreted from genetically-engineered *E. coli* mutants. For precise force measurements, careful preparations have been undertaken, including AFM tip apex characterization under SEM, as well as the calibration procedures necessary for precise force measurements. The thesis includes a detailed discussion of data acquisition and analysis procedures regarding nanoindentation experiments. The detailed processing routine allows to reveal the substrate effect on the measured mechanical stiffness of the amyloid nanofibers. We then present AFM topographical images revealing the morphological differences between different types of samples, as well as a statistical comparison of Young's modulus values associated with each sample type. Our experiments lead us to conclude that (i) the Linker-modified version of the CsgB protein plays a key role in augmenting the mechanical stiffness of amyloid nanofibers and (ii) the CsgA protein is needed for the formation of long-range, low-porosity biofilm backbones. To sum up, our results suggest that bacterial functional amyloid nanofibers could emerge as a flexible platform for various applications at the interface of bio- and nanotechnology.

It should be mentioned that additional experiments are needed to fully evaluate the dynamic behavior of such material systems, especially in their native liquid environment. Additionally, adhesive properties of genetically-tuned amyloid nanofibers can be compared and contrasted via force spectroscopy, for potential applications as functional biological scaffolds for nano-sized objects and devices.

Bibliography

[1] Feynman, R. P., There's plenty of room at the bottom. *Engineering and Science* 1960**,** *23* (5), 22-36.

[2] Bouju, X.; Joachim, C.; Girard, C., Single-atom motion during a lateral STM manipulation. *Physical Review B* 1999**,** *59* (12), R7845.

[3] Ashkin, A.; Dziedzic, J.; Yamane, T., Optical trapping and manipulation of single cells using infrared laser beams. *Nature* 1987**,** *330* (6150), 769-771.

[4] Sikorski, R. S.; Hieter, P., A system of shuttle vectors and yeast host strains designed for efficient manipulation of DNA in Saccharomyces cerevisiae. *Genetics* 1989**,** *122* (1), 19-27.

[5] https://www.ibiology.org

[6] Andrianantoandro, E.; Basu, S.; Karig, D. K.; Weiss, R., Synthetic biology: new engineering rules for an emerging discipline. *Molecular Systems Biology* 2006**,** *2*, 2006.0028.

[7] Govi, G., The compound microscope invented by Galileo. *Journal of the Royal Microscopical Society* 1889**,** *9*, 574-98.

[8] Baker, W. E. W., Origin and development of the microscope: as illustrated by catalogues of the instruments and accessories, in *Collections of the Royal Microscopical Society*. *The Royal Microscopical Society*, London: 1928.

[9] http://www.history-of-the-microscope.org/hans-lippershey-invented-the-telescope.php

[10] http://www.museogalileo.it/

[11] Ford, B. J., Images of science: a history of scientific illustration. *Oxford University Press,* New York: 1993.

[12] Hooke, R., Micrographia: or some physiological descriptions of minute bodies made by magnifying glasses, with observations and inquiries thereupon. *Jo. Martin and Ja. Allestry*, London: 1665.

[13] Gest, H., The discovery of microorganisms by Robert Hooke and Antoni Van Leeuwenhoek, fellows of the Royal Society. *Notes and Records of the Royal Society* 2004**,** *58* (2), 187-201.

[14] Lister, J. J. On Some Properties in Achromatic Object-Glasses Applicable to the Improvement of the Microscope. *The Royal Society*, London: 1815; pp 399-401.

[15] Mazzarello, P., A unifying concept: the history of cell theory. *Nature Cell Biology* 1999**,** *1* (1), E13-E15.

[16] Abbe, E., The Relation of Aperture and Power in the Microscope (continued). *Journal of the Royal Microscopical Society* 1883, *3* (6), 790-812.

[17] Abbe, E., Note on the Proper Definition of the Amplifying Power of a Lens or Lens-system. *Journal of Microscopy* 1884, *4* (3), 348-351.

[18] Koehler, A., Lighting system for cinematographs. *Google Patents*: 1915.

[19] Hell, S. W.; Wichmann, J., Breaking the diffraction resolution limit by stimulated emission: stimulated-emission-depletion fluorescence microscopy. *Optics Letters* 1994, *19* (11), 780-782.

[20] Masters, B. R., History of the electron microscope in cell biology, in *Encyclopedia of Life Sciences*. *John Wiley & Sons*, Chicester: 2009.

[21] Goldstein, J.; Newbury, D. E.; Echlin, P.; Joy, D. C.; Romig Jr, A. D.; Lyman, C. E.; Fiori, C.; Lifshin, E., Scanning electron microscopy and X-ray microanalysis. *Springer Science & Business Media*, New York: 2003.

[22] https://www.britannica.com/technology/scanning-electron-microscope

[23] Binnig, G.; Rohrer, H., Scanning tunneling microscopy—from birth to adolescence. *Reviews of Modern Physics* 1987, *59* (3), 615.

[24] Bennett, H.; Porteus, J., Relation between surface roughness and specular reflectance at normal incidence. *JOSA* 1961, *51* (2), 123-129.

[25] Young, R. D., Field emission ultramicrometer. *Review of Scientific Instruments* 1966, *37* (3), 275-278.

[26] Young, R.; Ward, J.; Scire, F., The topografiner: an instrument for measuring surface microtopography. *Review of Scientific Instruments* 1972, *43* (7), 999-1011.

[27] Binnig, G.; Rohrer, H.; Gerber, C.; Weibel, E., Tunneling through a controllable vacuum gap. *Applied Physics Letters* 1982, *40* (2), 178-180.

[28] http://www.wikiwand.com/en/Scanning_tunneling_microscope

[29] Binnig, G.; Quate, C. F.; Gerber, C., Atomic force microscope. *Physical Review Letters* 1986, *56* (9), 930.

[30] Eaton, P.; West, P., Atomic force microscopy. *Oxford University Press*, Oxford: 2010.

[31] Hansma, P.; Elings, V.; Marti, O.; Bracker, C., Scanning tunneling microscopy and atomic force microscopy: application to biology and technology. *Science* 1988, *242* (4876), 209-216.

[32] Drake, B.; Prater, C.; Weisenhorn, A.; Gould, S.; Albrecht, T., Imaging crystals, polymers, and processes in water with the atomic force microscope. *Science* 1989, *243* (4898), 1586.

[33] Butt, H.-J., Measuring electrostatic, van der Waals, and hydration forces in electrolyte solutions with an atomic force microscope. *Biophysical Journal* 1991, *60* (6), 1438.

[34] Radmacher, M.; Fritz, M.; Hansma, P. K., Imaging soft samples with the atomic force microscope: gelatin in water and propanol. *Biophysical Journal* 1995, *69* (1), 264.

[35] Kasas, S.; Thomson, N. H.; Smith, B. L.; Hansma, H. G.; Zhu, X.; Guthold, M.; Bustamante, C.; Kool, E. T.; Kashlev, M.; Hansma, P. K., Escherichia coli RNA polymerase activity observed using atomic force microscopy. *Biochemistry* 1997, *36* (3), 461-468.

[36] Robichon, D.; Girard, J.-C.; Cenatiempo, Y.; Cavellier, J.-F., Atomic force microscopy imaging of dried or living bacteria. *Comptes Rendus de l'Academie des Sciences-Series III-Sciences de la Vie* 1999, *322* (8), 687-693.

[37] Müller, D. J.; Janovjak, H.; Lehto, T.; Kuerschner, L.; Anderson, K., Observing structure, function and assembly of single proteins by AFM. *Progress in Biophysics and Molecular Biology* 2002, *79* (1), 1-43.

[38] Müller, D. J.; Anderson, K., Biomolecular imaging using atomic force microscopy. *Trends in Biotechnology* 2002, *20* (8), S45-S49.

[39] Kalle, W.; Strappe, P., Atomic force microscopy on chromosomes, chromatin and DNA: a review. *Micron* 2012, *43* (12), 1224-1231.

[40] Müller, D. J.; Dufrene, Y. F., Atomic force microscopy as a multifunctional molecular toolbox in nanobiotechnology. *Nature Nanotechnology* 2008, *3* (5), 261-269.

[41] Volle, C. B.; Ferguson, M. A.; Aidala, K. E.; Spain, E. M.; Núñez, M. E., Spring constants and adhesive properties of native bacterial biofilm cells measured by atomic force microscopy. *Colloids and Surfaces B: Biointerfaces* 2008, *67* (1), 32-40.

[42] Domke, J.; Radmacher, M., Measuring the elastic properties of thin polymer films with the atomic force microscope. *Langmuir* 1998, *14* (12), 3320-3325.

[43] Doktycz, M.; Sullivan, C.; Hoyt, P.; Pelletier, D.; Wu, S.; Allison, D., AFM imaging of bacteria in liquid media immobilized on gelatin coated mica surfaces. *Ultramicroscopy* 2003, *97* (1), 209-216.

[44] Guo, S.; Akhremitchev, B. B., Packing density and structural heterogeneity of insulin amyloid fibrils measured by AFM nanoindentation. *Biomacromolecules* 2006, *7* (5), 1630-1636.

[45] Müller, D. J.; Heymann, J. B.; Oesterhelt, F.; Möller, C.; Gaub, H.; Büldt, G.; Engel, A., Atomic force microscopy of native purple membrane. *Biochimica et Biophysica Acta (BBA)-Bioenergetics* 2000, *1460* (1), 27-38.

[46] Kuznetsov, Y. G.; Malkin, A.; Lucas, R.; Plomp, M.; McPherson, A., Imaging of viruses by atomic force microscopy. *Journal of General Virology* 2001, *82* (9), 2025-2034.

[47] Pyrgiotakis, G.; Blattmann, C. O.; Demokritou, P., Real-time nanoparticle–cell interactions in physiological media by atomic force microscopy. *ACS Sustainable Chemistry & Engineering* 2014, *2* (7), 1681-1690.

[48] Touhami, A.; Jericho, M. H.; Boyd, J. M.; Beveridge, T. J., Nanoscale characterization and determination of adhesion forces of Pseudomonas aeruginosa pili by using atomic force microscopy. *Journal of Bacteriology* 2006, *188* (2), 370-377.

[49] Lee, H.; Scherer, N. F.; Messersmith, P. B., Single-molecule mechanics of mussel adhesion. *Proceedings of the National Academy of Sciences* 2006, *103* (35), 12999-13003.

[50] Iyer, S.; Gaikwad, R.; Subba-Rao, V.; Woodworth, C.; Sokolov, I., Atomic force microscopy detects differences in the surface brush of normal and cancerous cells. *Nature Nanotechnology* 2009, *4* (6), 389-393.

[51] Gilbert, Y.; Deghorain, M.; Wang, L.; Xu, B.; Pollheimer, P. D.; Gruber, H. J.; Errington, J.; Hallet, B.; Haulot, X.; Verbelen, C., Single-molecule force spectroscopy and imaging of the vancomycin/D-Ala-D-Ala interaction. *Nano Letters* 2007, *7* (3), 796-801.

[52] Dufrêne, Y. F., Atomic force microscopy and chemical force microscopy of microbial cells. *Nature Protocols* 2008, *3* (7), 1132-1138.

[53] Simon, A.; Durrieu, M.-C., Strategies and results of atomic force microscopy in the study of cellular adhesion. *Micron* 2006, *37* (1), 1-13.

[54] Hinterdorfer, P.; Dufrêne, Y. F., Detection and localization of single molecular recognition events using atomic force microscopy. *Nature Methods* 2006, *3* (5), 347-355.

[55] Dupres, V.; Verbelen, C.; Dufrêne, Y. F., Probing molecular recognition sites on biosurfaces using AFM. *Biomaterials* 2007, *28* (15), 2393-2402.

[56] Staunton, J. R.; Doss, B. L.; Lindsay, S.; Ros, R., Correlating confocal microscopy and atomic force indentation reveals metastatic cancer cells stiffen during invasion into collagen I matrices. *Scientific Reports* 2016, *6*, 19686.

[57] Odermatt, Pascal D., et al., High-resolution correlative microscopy: bridging the gap between single molecule localization microscopy and atomic force microscopy. *Nano Letters* 2015, 15 (8), 4896-4904.

[58] Kodera, N.; Yamamoto, D.; Ishikawa, R.; Ando, T., Video imaging of walking myosin V by high-speed atomic force microscopy. *Nature* 2010, *468* (7320), 72-76.

[59] Colom, A.; Casuso, I.; Rico, F.; Scheuring, S., A hybrid high-speed atomic force–optical microscope for visualizing single membrane proteins on eukaryotic cells. *Nature Communications* 2013, *4*, 2155.

[60] Suzuki, Y.; Sakai, N.; Yoshida, A.; Uekusa, Y.; Yagi, A.; Imaoka, Y.; Ito, S.; Karaki, K.; Takeyasu, K., High-speed atomic force microscopy combined with inverted optical microscopy for studying cellular events. *Scientific Reports* 2013, *3*, 2131.

[61] Preiner, J.; Kodera, N.; Tang, J.; Ebner, A.; Brameshuber, M.; Blaas, D.; Gelbmann, N.; Gruber, H. J.; Ando, T.; Hinterdorfer, P., IgGs are made for walking on bacterial and viral surfaces. *Nature Communications* 2014, *5*, 4394.

[62] Dufrêne, Y. F., Recent progress in the application of atomic force microscopy imaging and force spectroscopy to microbiology. *Current Opinion in Microbiology* 2003, *6* (3), 317-323.

[63] McKhann, G.; Drachman, D.; Folstein, M.; Katzman, R.; Price, D.; Stadlan, E. M., Clinical diagnosis of Alzheimer's disease Report of the NINCDS-ADRDA Work Group* under the auspices of Department of Health and Human Services Task Force on Alzheimer's Disease. *Neurology* 1984, *34* (7), 939-939.

[64] Chiti, F.; Dobson, C. M., Protein misfolding, functional amyloid, and human disease. *Annu. Rev. Biochem.* 2006, *75*, 333-366.

[65] Ivanova, M. I.; Sievers, S. A.; Sawaya, M. R.; Wall, J. S.; Eisenberg, D., Molecular basis for insulin fibril assembly. *Proceedings of the National Academy of Sciences* 2009, *106* (45), 18990-18995.

[66] Nelson, R.; Sawaya, M. R.; Balbirnie, M.; Madsen, A. Ø.; Riekel, C.; Grothe, R.; Eisenberg, D., Structure of the cross-β spine of amyloid-like fibrils. *Nature* 2005, *435* (7043), 773-778.

[67] Sawaya, M. R.; Sambashivan, S.; Nelson, R.; Ivanova, M. I.; Sievers, S. A.; Apostol, M. I.; Thompson, M. J.; Balbirnie, M.; Wiltzius, J. J.; McFarlane, H. T., Atomic structures of amyloid cross-β spines reveal varied steric zippers. *Nature* 2007, *447* (7143), 453-457.

[68] Wiltzius, J. J.; Sievers, S. A.; Sawaya, M. R.; Cascio, D.; Popov, D.; Riekel, C.; Eisenberg, D., Atomic structure of the cross-β spine of islet amyloid polypeptide (amylin). *Protein Science* 2008, *17* (9), 1467-1474.

[69] Wiltzius, J. J.; Landau, M.; Nelson, R.; Sawaya, M. R.; Apostol, M. I.; Goldschmidt, L.; Soriaga, A. B.; Cascio, D.; Rajashankar, K.; Eisenberg, D., Molecular mechanisms for protein-encoded inheritance. *Nature Structural & Molecular Biology* 2009, *16* (9), 973-978.

[70] Gebbink, M. F.; Claessen, D.; Bouma, B.; Dijkhuizen, L.; Wösten, H. A., Amyloids—a functional coat for microorganisms. *Nature Reviews Microbiology* 2005, *3* (4), 333-341.

[71] Wang, X.; Hammer, N. D.; Chapman, M. R., The molecular basis of functional bacterial amyloid polymerization and nucleation. *Journal of Biological Chemistry* 2008, *283* (31), 21530-21539.

[72] http://wavefunction.fieldofscience.com/2011/08/barrier-to-amyloid-formation-is-kinetic.html.

[73] Greenwald, J.; Riek, R., Biology of amyloid: structure, function, and regulation. *Structure* 2010, *18* (10), 1244-1260.

[74] Shewmaker, F.; McGlinchey, R. P.; Wickner, R. B., Structural insights into functional and pathological amyloid. *Journal of Biological Chemistry* 2011, *286* (19), 16533-16540.

[75] Smith, J. F.; Knowles, T. P.; Dobson, C. M.; MacPhee, C. E.; Welland, M. E., Characterization of the nanoscale properties of individual amyloid fibrils. *Proceedings of the National Academy of Sciences* 2006, *103* (43), 15806-15811.

[76] Barnhart, M. M.; Chapman, M. R., Curli biogenesis and function. *Annu. Rev. Microbiol.* 2006, *60*, 131-147.

[77] Hammer, N. D.; Schmidt, J. C.; Chapman, M. R., The curli nucleator protein, CsgB, contains an amyloidogenic domain that directs CsgA polymerization. *Proceedings of the National Academy of Sciences* 2007, *104* (30), 12494-12499.

[78] Baykara, M. Z.; Schwendemann, T. C.; Altman, E. I.; Schwarz, U. D., Three-Dimensional Atomic Force Microscopy–Taking Surface Imaging to the Next Level. *Advanced Materials* 2010, *22* (26-27), 2838-2853.

[79] Abdelwahab, M. T.; Kalyoncu, E.; Onur, T.; Baykara, M. Z.; Seker, U. O. S., Genetically-Tunable Mechanical Properties of Bacterial Functional Amyloid Nanofibers. *Langmuir* 2017, *33* (17), 4337–4345.

[80] Gaboriaud, F.; Dufrêne, Y. F., Atomic force microscopy of microbial cells: application to nanomechanical properties, surface forces and molecular recognition forces. *Colloids and Surfaces B: Biointerfaces* 2007, *54* (1), 10-19.

[81] Sader, J. E.; Larson, I.; Mulvaney, P.; White, L. R., Method for the calibration of atomic force microscope cantilevers. *Review of Scientific Instruments* 1995, *66* (7), 3789-3798.

[82] Louros, N. N.; Bolas, G. M. P.; Tsiolaki, P. L.; Hamodrakas, S. J.; Iconomidou, V. A., Intrinsic aggregation propensity of the CsgB nucleator protein is crucial for curli fiber formation. *Journal of Structural Biology* 2016, *195* (2), 179-189.

[83] Hammer, N. D.; McGuffie, B. A.; Zhou, Y. Z.; Badtke, M. P.; Reinke, A. A.; Brannstrom, K.; Gestwicki, J. E.; Olofsson, A.; Almqvist, F.; Chapman, M. R.,

The C-Terminal Repeating Units of CsgB Direct Bacterial Functional Amyloid Nucleation. *Journal of Molecular Biology* 2012, *422* (3), 376-389.

[84] Knowles, T. P.; Fitzpatrick, A. W.; Meehan, S.; Mott, H. R.; Vendruscolo, M.; Dobson, C. M.; Welland, M. E., Role of intermolecular forces in defining material properties of protein nanofibrils. *Science* 2007, *318* (5858), 1900-1903.

[85] Knowles, T. P.; Buehler, M. J., Nanomechanics of functional and pathological amyloid materials. *Nature Nanotechnology* 2011, *6* (8), 469-479.

[86] Adamcik, J.; Berquand, A.; Mezzenga, R., Single-step direct measurement of amyloid fibrils stiffness by peak force quantitative nanomechanical atomic force microscopy. *Applied Physics Letters* 2011, *98* (19), 193701.

[87] Adamcik, J.; Lara, C.; Usov, I.; Jeong, J. S.; Ruggeri, F. S.; Dietler, G.; Lashuel, H. A.; Hamley, I. W.; Mezzenga, R., Measurement of intrinsic properties of amyloid fibrils by the peak force QNM method. *Nanoscale* 2012, *4* (15), 4426-4429.

[88] Adamcik, J.; Jung, J.-M.; Flakowski, J.; De Los Rios, P.; Dietler, G.; Mezzenga, R., Understanding amyloid aggregation by statistical analysis of atomic force microscopy images. *Nature Nanotechnology* 2010, *5* (6), 423-428.

[89] Adamcik, J.; Mezzenga, R., Proteins fibrils from a polymer physics perspective. *Macromolecules* 2011, *45* (3), 1137-1150.

[90] Chen, A. Y.; Deng, Z. T.; Billings, A. N.; Seker, U. O. S.; Lu, M. Y.; Citorik, R. J.; Zakeri, B.; Lu, T. K., Synthesis and patterning of tunable multiscale materials with engineered cells. *Nature Materials* 2014, *13* (5), 515-523.

[91] Seker, U. O. S.; Chen, A. Y.; Citorik, R. J.; Lu, T. K., Synthetic Biogenesis of Bacterial Amyloid Nanomaterials with Tunable Inorganic–Organic Interfaces and Electrical Conductivity. *ACS Synthetic Biology* 2017, *6* (2), 266-275.

[92] Seker, U. O. S.; Mutlugun, E.; Hernandez-Martinez, P. L.; Sharma, V. K.; Lesnyak, V.; Gaponik, N.; Eychmüller, A.; Demir, H. V., Bio-nanohybrids of quantum dots and photoproteins facilitating strong nonradiative energy transfer. *Nanoscale* 2013, *5* (15), 7034-7040.

[93] Zhong, C.; Gurry, T.; Cheng, A. A.; Downey, J.; Deng, Z.; Stultz, C. M.; Lu, T. K., Strong underwater adhesives made by self-assembling multi-protein nanofibres. *Nature Nanotechnology* 2014, *9* (10), 858-866.